

# Rydberg Atoms in THz Fields

Master Thesis in Atomic Physics

by

Jørgen Johansen Rørstad

November, 2015



Department of Physics and Technology

University of Bergen

Norway

*A physicist is just an atom's way of looking at itself*

*Niels Bohr*

## Abstract

Rydberg atoms are highly excited atoms with bizarre and exotic properties such as huge orbits and exaggerated sensitivity to fields. In this study we examine these atoms using classical methods. We present the classical trajectory Monte Carlo (CTMC) method, where the microcanonical distribution is used. This is a model based on the microcanonical ensemble from statistical mechanics and can be used to initialize the desired atomic system. The systems are propagated by classical equations solved numerically.

Recent experiment found ionization probabilities of excited sodium atoms under the influence of a single-cycle THz field. Energy distributions of the electrons from ionized states were obtained. We make corresponding classical calculations and compare results. For field strengths corresponding to low ionization probabilities we see a  $n^{-3}$  scaling behaviour in experimental results as well as in classical calculations. For higher field strengths the results diverge, with classical results scaling as  $n^{-4}$  and experimental results as  $n^{-3}$ . Further calculations show that states require stronger fields to ionize at very high  $n$ . Ionization probabilities for states with various angular momentum  $\ell$  were compared and states with relatively low  $\ell$  were found to ionize before states with relatively high  $\ell$ . Energy distribution of electrons from ionized states were compared with experimental results and the underlying trend were found to be in some agreement. The current classical method was however unable to reproduce detailed properties of the distributions. Further calculations were done for energy distributions of hydrogen and sodium in various states and results suggests that core scattering plays a role in these interactions. Momenta and positions of electrons from ionized states as a function of time are for high  $n$  found to agree with analytical calculations corresponding to a free particle in a field. Investigations of single electron trajectories are made to glean insights into ionization mechanisms.

Corresponding author: jorgen.j.rorstad@gmail.com

## Acknowledgements

I am indebted to many people for the realization of this thesis for the degree of Master of Science. During the course of my work here I have been amazed and inspired by the kindness and helpfulness shown by the many good people at the optics and atomic physics group here at the Department.

First I would like to thank my supervisor Jan Petter Hansen. His door has always been open whenever I have had questions. He has been a tremendous support and has strived to ensure that I would produce quality work.

Another person deserving special mention is Ladislav Kocbach. He has spent many hours discussing physics and working out improvements with me, often on his own initiative, for which I am immensely grateful. His altruism and love for physics is truly inspiring to me.

The members of our group here in Bergen have made my stay deeply enjoyable. I owe special thanks to Aleksander Simonsen for taking time to advice me. He is an excellent teacher and a true workhorse. Thanks to Arne Kristoffersen for many entertaining lunches and of course the occasional prank. Also thanks to Yi-Chun Chen, for her remarkable generosity and for the hosting of many social events. And thanks to Michaela Chovancova and Hicham Agueny who works on parallel projects for their interest in my work.

I would like to thank my friends and fellow students at the Department, many of whom I have known since I first started here 5 years ago. Many hours have been spent together immersed in interesting discussions, studying for exams or drinking beer in  $\hbar$ . Thanks to the brilliant Kristoffer Johansen for his comprehensive review of my thesis, which was incredibly helpful.

A huge thanks to Vegard Børve SørDAL for introducing me to physics. Without him I might never have come to know the field which I now love. Thanks to my dear friend Magnus Hoff Rishaug for the countless good times we have had in Bergen up through the years.

Special thanks to Katérina Verteletsky, for her extremely thorough and delightfully candid critique of my thesis and for the moral support she has given me while writing it.

Last, but not least, I would like to thank my parents, Elisa Rørstad and Terje Wenum. Their unconditional support during all my years of studying has been invaluable.

Jørgen Johansen Rørstad  
Bergen, November 2015

# Table of Contents

<b>1</b>	<b>Introduction</b>	<b>5</b>
1.1	Monte Carlo Method . . . . .	6
1.2	Rydberg Atoms . . . . .	7
1.3	Outline . . . . .	7
<b>2</b>	<b>Quantum Mechanics</b>	<b>11</b>
2.1	Schrödinger Equation . . . . .	11
2.1.1	Basis Expansion . . . . .	12
2.1.2	Light-Matter Interaction . . . . .	12
2.2	Example: Soft Coulomb Potential in One Dimension . . . . .	14
2.3	Time Propagation . . . . .	19
2.3.1	Eigenstate Expansion . . . . .	19
2.3.2	Discretization . . . . .	20
<b>3</b>	<b>CTMC - Classical Trajectory Monte Carlo</b>	<b>23</b>
3.1	Sampling . . . . .	23
3.1.1	Uniform Density Covering of a Disc . . . . .	23
3.1.2	Uniform Density Covering of a Sphere . . . . .	25
3.2	Initial Conditions . . . . .	26
3.2.1	The Microcanonical Distribution . . . . .	26
3.2.2	Random Number Generation . . . . .	28
3.2.3	Comparison . . . . .	29
3.2.4	Potentials . . . . .	31
3.2.5	Angular Momentum . . . . .	31
3.2.6	Energies . . . . .	32
3.3	Dynamics . . . . .	33
3.3.1	Free Electron . . . . .	34
3.4	Analysis . . . . .	35

<b>4</b>	<b>Results and Discussion</b>	<b>37</b>
4.1	Experiment . . . . .	37
4.1.1	Pulse . . . . .	38
4.1.2	Experimental Results . . . . .	39
4.2	CTMC - 3D . . . . .	43
4.2.1	Ionization Probabilities; Simulations versus Experiment . . . . .	43
4.2.2	Ionization Probability Landscapes . . . . .	47
4.2.3	Orbital Angular Momentum . . . . .	51
4.2.4	Free Electron Energy Distribution . . . . .	54
4.2.5	Temporal Behaviour . . . . .	62
4.2.6	Final State Momentum Distribution . . . . .	67
4.2.7	Individual Electron Trajectories . . . . .	69
<b>5</b>	<b>Conclusion and Outlook</b>	<b>75</b>

# List of Figures

2.1	Lowest bound states ( $n \in \{1, 2, 3\}$ ) of the soft coulomb potential . . . . .	18
2.2	$n \in \{10, 20, 60\}$ states of the soft coulomb potential . . . . .	18
2.3	$n \in \{10, 20, 60\}$ states the soft coulomb potential influenced by weak field	19
2.4	$ \Psi ^2$ versus $x$ for an electron initially in state $n = 10$ under the influence of an electric field . . . . .	21
2.5	$ \Psi ^2$ versus $x$ for an electron initially in state $n = 20$ under the influence of an electric field . . . . .	22
3.1	Nonuniform and uniform sampling of points inside a disc . . . . .	24
3.2	CTMC - Probability density for $\mathbf{r}$ in H(1s). . . . .	29
3.3	CTMC - Probability density for $\mathbf{p}$ in H(1s) . . . . .	30
3.4	Angular momenta of the microcanonical distribution . . . . .	32
4.1	a) Maximum momentum transfer from field to electrons, b) Experimental single-cycle THz waveform . . . . .	38
4.2	Experimental ionization probabilities; scaled, stretched and superimposed curves . . . . .	40
4.3	Peak THz field required for 10% ionization as a function of $n$ ; experimental results. . . . .	41
4.4	Electron energy distributions for ionized states; experimental results. . .	42
4.5	Calculated ionization probabilities for sodium atoms as a function of the scaled relative peak field intensity $F_{max}$ of an asymmetric pulse. . . . .	44
4.6	Required peak field strength for 10% and 80% ionization probability for sodium in $nd$ state. . . . .	45
4.7	Calculated ionization probabilities for sodium atoms as a function of the scaled relative peak field intensity $F_{max}$ of a symmetric pulse. . . . .	46
4.8	Ionization probabilities of hydrogen as a function of field strength for low-lying states; symmetric pulse . . . . .	47
4.9	Ionization probabilities of hydrogen as a function of field strength for high $n$ states; symmetric pulse . . . . .	48
4.10	Ionization probabilities of hydrogen as a function of field strength for states with a broad $n$ range; asymmetric pulse . . . . .	49

4.11	Threshold ionization field strength for all three elements with a broad $n$ range . . . . .	50
4.12	Ionization probabilities versus maximum field strength for hydrogen with various angular momenta $\ell$ . . . . .	51
4.13	Ionization probabilities versus maximum field strength for sodium and lithium with initial $n = 6$ and various initial angular momentum $\ell$ . . . .	52
4.14	Ionization probabilities versus maximum field strength for sodium and lithium with initial $n = 12$ and various initial angular momentum $\ell$ . . .	53
4.15	Energy distribution of electrons from ionized states of sodium initially in a $n = \{6, 9, 15\}$ state. Computational results compared with experimental results. . . . .	55
4.16	Energy distribution of electrons from ionized states of hydrogen and sodium atoms initially in a $n = 6$ state; relatively low field strength . . .	56
4.17	Energy distribution of electrons from ionized states of from hydrogen and sodium atoms initially in a $n = 6$ state; relatively high field strength . . .	57
4.18	Energy distribution of electrons from ionized states of hydrogen and sodiums initially in a $n = 9$ state. . . . .	59
4.19	Energy distribution of electrons from ionized states of hydrogen and sodiums initially in a $n = 12$ state. . . . .	60
4.20	Energy distribution of electrons from ionized states of hydrogen and sodiums initially in a $n = 15$ state. . . . .	60
4.21	$\langle z \rangle$ as a function of time for hydrogen in various initial $n$ states, with peak field strength of the symmetric incident field $E = 600$ kV/cm. . . .	62
4.22	$\langle p_z \rangle$ as a function of time for hydrogen in various initial $n$ states, with peak field strength of the symmetric incident field $E = 600$ kV/cm. . . .	63
4.23	$\langle z \rangle$ as a function of time for the $H(9d)$ state . . . . .	64
4.24	$\langle p_z \rangle$ as a function of time for the $H(9d)$ state . . . . .	65
4.25	$\langle z \rangle$ and $\langle p_z \rangle$ as a function of time for the $Na(9d)$ state . . . . .	66
4.26	Surface plots of final state momentum distribution of hydrogen initially in $n \in \{6, 9\}$ states, subjected to pulse with peak field strength $E = 600$ kV/cm. . . . .	67
4.27	Surface plots of final state momentum distribution of hydrogen initially in $n \in \{12, 15\}$ states, subjected to pulse with peak field strength $E = 600$ kV/cm. . . . .	68
4.28	Hydrogen electron trajectory; $n = 9$ , no field . . . . .	69
4.29	Hydrogen electron trajectory; $n = 6$ , $E = 800$ kV/cm . . . . .	70
4.30	Hydrogen electron trajectory; $n = 9$ , $E = 400$ kV/cm . . . . .	71
4.31	Hydrogen electron trajectory; $n = 15$ , $E = 50$ kV/cm. . . . .	71
4.32	Hydrogen electron trajectory; $n = 15$ , $E = 300$ kV/cm. . . . .	72
4.33	Sodium electron trajectory; $n = 9$ , $E = 300$ kV/cm . . . . .	72



# Nomenclature

## Abbreviations

BO Born-Oppenheimer

CTMC Classical Trajectory Monte Carlo

FNA Fixed Nuclei Approximation

QM Quantum Mechanics

TDSE Time-Dependent Schrödinger Equation

TISE Time-Independent Schrödinger Equation

## Constants

$\alpha = 1/137.036$  Fine structure constant

$\epsilon_0 = 8.85419 \times 10^{-12} \text{ Fm}^{-1}$  Permittivity of free space

$\hbar = 1.05457 \times 10^{-34} \text{ Js}$  Reduced Plank's constant

$\mu_0 = 1.25664 \times 10^{-6} \text{ Hm}^{-1}$  Permeability of free space

$c = 2.99792 \times 10^8 \text{ ms}^{-1}$  Speed of light in vacuum

$e = 1.60218 \times 10^{-19} \text{ C}$  Elementary charge

$h = 6.62607 \times 10^{-34} \text{ Js}$  Plank's constant

$m_e = 9.10938 \times 10^{-31} \text{ kg}$  Electron mass

$M_p = 1.67262 \times 10^{-27} \text{ kg}$  Proton mass



# Chapter 1

## Introduction

The year is 460 BC. This may very well have been around the time when the atom first made its leap in to the human consciousness, more specifically to the mind of the Greek philosopher Democritus. Some say that as he was walking on a beach a thought struck him. The beach, so large and seemingly continuous when viewed from a distance, is upon closer inspection revealed to consist of a vast amount of tiny grains. Could this also be the case for the macroscopic world? He postulated that if you divide something enough times you would eventually end up with an indivisible particle. And so the atom was given its name, from the Greek word *atomos*, which means 'that which cannot be split'.

Unfortunately some of his esteemed contemporaries did not hold his theory in high regard. Aristotle, whose word carried considerable weight, thought it held no merit and disregarded it outright. He supported the more popular theory of the four elements, which was widely accepted by the Greek philosophers and prevailed for centuries.

And so the atom continued its existence, most likely indifferent to its obscurity in human society. The comeback was arranged in the early 1800s, by English chemist John Dalton, and since then its place in science has been cemented. After going through intermediate stages such as the plum pudding model it finally converged to an entity consisting of neutrons, protons and electrons, currently best described by quantum mechanics (QM).

Newton's classical mechanics were largely abandoned in the 1920s when the physicists in the world turned their attention to the new quantum mechanics. But there was a price to pay for the accuracy of QM. Only the simplest problems, e.g. the hydrogen atom, are analytically solvable; and the computational complexity faced when dealing with more advanced systems is potentially overwhelming even for the most advanced modern computers.

This brings us closer to the topic of this study. Certain physicists [1, 2] realized that classical mechanics should not be discounted entirely, as it could in certain situations provide results that agreed with experimental results, at a fraction of the computational cost. The idea was to use an ensemble of a large amount of classical particles. Certain

properties of this ensemble could be made to mimic their quantum mechanical counterpart.

## 1.1 Monte Carlo Method

The modern version of the Monte Carlo method was conceived by Stanislaw Ulam in 1946 [2]. Enrico Fermi had used a similar technique a decade earlier, when studying neutron diffusion, but he did not publish anything on the subject [3]. The usefulness of the method was at this time limited by its lengthy and tedious calculations. The change came with the advent of the first electronic computer, the ENIAC. Ulam realized that the necessary calculating power was now available, and proceeded to revive the statistical techniques. He discussed the idea with John von Neumann, who welcomed it with great enthusiasm. Together they pioneered the method. The Monte Carlo name was suggested by Nicholas Metropolis, and is a reflection of its probabilistic essence and related to the fact that Ulam's uncle had an affinity for gambling.

There exists a variety of different Monte Carlo methods, but they all adhere to a certain pattern. Initially a domain of inputs is defined. The chosen domain must be appropriate for the specific problem at hand. Next, random inputs based on a probability distribution over the domain are generated. Desired deterministic calculations are performed on the generated inputs, and finally the results of all the calculations are combined.

The classical trajectory Monte Carlo (CTMC) method started with Hirschfelder in 1936, in a paper on chemical reactions involving hydrogen [4]. In atomic physics, however, the development of quantum theory had lead to a general neglect of classical methods. A paper by Gryzinski [5] in 1959 marked the comeback of these methods; he showed that they could be used to calculate approximate cross section for a wide variety of processes.

A few years later Abrines and Percival [6] took a major step towards adapting a CTMC method for atomic physics. They proposed that the electronic configuration of the target atom could be adequately represented by a microcanonical distribution. Other recent papers [7, 8] on the topic had made two basic approximations:

- *The classical approximation*, which states that the particles are subject to Newtonian laws during collisions.
- *The impulse approximation*, which states that a collision involving several particles is approximated using a two-body collision for each electron of the atom.

Only the classical approximation is made in the method of Abrines and Percival.

The method was further refined for general central interactions by Reinhold and Falcón [9] in 1986. The improvement was mainly a numerical one, removing the encumbering necessity of calculating the Kepler orbit of the electrons. The work herein is based on both of these schemes.

## 1.2 Rydberg Atoms

A move from the microscopic to the macroscopic also entails a move from quantum mechanics to classical mechanics. The exact point where one approach becomes impractical and the other becomes practical is impossible to pin down, but in the borderlands between the two regimes lies the Rydberg atom [10].

A Rydberg atom is a highly excited atom, with a large principal quantum number  $n$ . Rydberg atoms have many exotic properties that make them ideal candidates for exploring atomic dynamics. These properties include potentially huge orbits, long lifetimes, exaggerated sensitivity to electric and magnetic fields and high state densities.

Historically, Bohr's hydrogen atom played an important role in the development of the concept of the Rydberg atom [11]. In high  $n$ , the orbital radii of the electron around the Bohr atom increases as  $n^2$  and its binding energies decreases as  $n^{-2}$ . In Bohr's model it was clear that the valence electron of the Rydberg atom was weakly bound and had a large orbit, and that it should have bizarre properties.

In spite of its interesting properties, the Rydberg atom did not receive a lot of attention until the 1970s. This was likely due to the development of quantum mechanics being an area of much greater interest, and also because there was no way to produce Rydberg atoms efficiently enough to conduct experiments on them.

The interest in Rydberg atoms really took off when it was discovered that they played an important part in real physical systems, e.g. in astrophysics. Transitions between states with very high  $n$  results in radio waves that can be detected on Earth. After the development of the tunable dye laser it was finally possible to excite a large number of atoms to desired energy levels with great precision.

Many of the properties from relatively low lying states were found to extrapolate to the higher states. However the most interesting discoveries were perhaps those peculiar to the Rydberg atom. The effects of electric fields on these atoms are dramatic. This is interesting in its own right, but it also allowed for novel techniques of detection and manipulation of the Rydberg atom.

Rydberg atoms offer the opportunity to conduct experiments that would normally be deemed impossible. Fascinating research has been done on these atoms, and there is likely more to come.

## 1.3 Outline

The aim of the present work is to examine the behaviour of Rydberg atoms in single-cycle THz fields. We begin in chapter 2 by presenting relevant theory of quantum mechanics and calculations on 1D systems. Quantum mechanics is currently the most accurate way to represent the systems, however the temporal and spatial dimensions of the systems considered are large, making 3D quantum calculations very challenging. This is an area

of active research for the group here at the University of Bergen. The bulk part of this thesis consists of results obtained from 3D CTMC. The theory of this method is given in chapter 3, where the topics include how to initialize a classical system, how to translate quantum mechanical concepts in appropriate classical analogues and how to propagate a classical system in time. In chapter 4 the results are shown. We start by presenting the experimental work, which served as part of the motivation for this thesis. Next we look at calculations for ionization probabilities of Rydberg atoms influenced by single-cycle pulses, the energy distribution of electrons from ionized states, electron behaviour as a function of time and finally we consider some individual electron trajectories. In chapter 5 we present the conclusions of the present work and suggestions for further research.

### Atomic units

The atomic unit system is often used in calculations on atomic length scales, and this system of units is given in Table 1.1 [12]. This system of units is obtained by setting the quantities  $m_e$ ,  $e$ ,  $\hbar$  and  $a_0$  equal to unity. Quantities that are given in atomic units are abbreviated by the symbol *a.u.*

Physical Unit	Unit	Physical origin	Value in SI units
Mass	$m$	Electron mass	$9.10938 \times 10^{-31}$ kg
Charge	$e$	Absolute value of the electron charge	$1.60218 \times 10^{-19}$ C
Angular Momentum	$\hbar$	The reduced Planck's constant	$1.05457 \times 10^{-34}$ J s <sup>-1</sup>
Length	$a_0$	Bohr radius for atomic hydrogen (with infinite nuclear mass)	$5.29177 \times 10^{-11}$ m
Velocity	$v_0 = \alpha c$	Magnitude of electron velocity in first Bohr orbit	$2.18769 \times 10^6$ ms <sup>-1</sup>
Momentum	$p_0 = mv_0$	Magnitude of electron momentum in the first Bohr orbit	$1.99285 \times 10^{-24}$ kg m s <sup>-1</sup>
Time	$\frac{a_0}{v_0}$	Time required for electron in first Bohr orbit to travel one Bohr radius	$2.41888 \times 10^{-17}$ s
Frequency	$\frac{v_0}{2\pi a_0}$	Angular frequency of electron in first Bohr orbit divided by $2\pi$	$6.57969 \times 10^{15}$ s <sup>-1</sup>
Energy	$\frac{e^2}{4\pi\epsilon_0 a_0}$	Twice the ionization potential of atomic hydrogen (with infinite nuclear mass)	$4.35974 \times 10^{-18}$ J
Electric field strength	$\frac{e}{(4\pi\epsilon_0)a_0^2}$	Strength of the Coulomb field experienced by an electron in the first Bohr orbit of atomic hydrogen (with infinite nuclear mass)	$5.14221 \times 10^{11}$ Vm <sup>-1</sup>

Table 1.1: Table of the atomic unit system and how the quantities are related to the SI system of units





# Chapter 2

## Quantum Mechanics

In this chapter a brief introduction to relevant parts of quantum mechanics will be given. Certain cumbersome derivations are avoided and the reader is instead directed to more comprehensive literature through references. We begin the chapter by introducing the Schrödinger equation. Next, light-matter interaction and gauge choices in the semi-classical picture are considered. After this we solve the time-independent Schrödinger equation (TISE) to obtain eigenstate wave functions and corresponding energy levels for the soft Coulomb potential. Finally, we discuss several methods for propagating a quantum mechanical system in time. Atomic units (see table 1.1) are used throughout this chapter.

### 2.1 Schrödinger Equation

The Schrödinger equation provides the means to determine the present and future state of a quantum mechanical system. It was published by Austrian physicist Erwin Schrödinger in 1926 [13]. The time-independent equation was developed first, and he used this to solve the eigenvalue problem for the hydrogen atom. In the same year he published the time-dependent form of the equation, which is considered to be the most general form. The Time Dependent Schrödinger equation (TDSE) is a partial differential equation that describes how the wave function of a system evolves in time. Its classical analogue is Newton's second law  $\mathbf{F} = m\mathbf{a}$  which, given initial conditions, can be used to determine the state of the system at a future time.

In classical mechanics the hamiltonian  $H$  expresses the total energy of the system. In quantum mechanics momentum and position are replaced by operators  $(\hat{p}, \hat{x}) \rightarrow (-i\frac{d}{dx}, x)$  turning the Hamiltonian into an operator acting on the wave function of the system. It is commonly expressed as a sum of the operators corresponding to kinetic and potential energies of a system as  $\hat{H} = \hat{T} + \hat{V}$ .

For non-relativistic systems in 1D the general form of the TDSE is

$$i\frac{\partial}{\partial t}\Psi(x,t) = \hat{H}\Psi(x,t), \quad (2.1)$$

where  $\Psi(x,t)$  is the wave function of the system,  $i$  is the imaginary unit and  $\hat{H}$  is the Hamiltonian operator.

For illustrative purposes we consider the case of a particle with mass  $m$  that is moving in one dimension and under the influence of a potential  $V(x,t)$ . The term representing the kinetic energy  $\hat{T}$  becomes

$$\hat{T} = -\frac{1}{2m} \frac{\partial^2}{\partial x^2} \quad (2.2)$$

and the Schrödinger equation is

$$i\frac{\partial}{\partial t}\Psi(x,t) = \left[ -\frac{1}{2m} \frac{\partial^2}{\partial x^2} + \hat{V}(x,t) \right] \Psi(x,t). \quad (2.3)$$

When the Hamiltonian is time independent, the TISE can be separated through  $\Psi(x,t) \rightarrow \psi(x)e^{iEt}$ , where  $E$  is the separation constant which we identify as the total energy. We then obtain the TISE for the stationary wave function  $\psi(x)$ :

$$\hat{H}\psi = E\psi \quad (2.4)$$

Equation (2.1) is only analytically solvable for certain relatively simple problems, e.g. square wells or the simple harmonic oscillator. When the system becomes sufficiently complex approximative methods are required.

### 2.1.1 Basis Expansion

We represent a given wave function as a linear combination of basis functions

$$\psi = \sum_{i=0}^{\infty} c_i \phi_i, \quad (2.5)$$

to precisely describe the original function an infinite number of basis functions must be used. In practice we can only use a finite number of basis functions,  $k$ , the summation limit changes as  $\infty \rightarrow k$ .

### 2.1.2 Light-Matter Interaction

The emergence of electromagnetism in the 19th century was one of the most important events in the history of physics. Great physicists such as Charles-Augustin de Coulomb, Carl Friedrich Gauss, André-Marie Ampère, Michael Faraday and others made the vital

contributions that allowed James Clerk Maxwell to compose his famous set of equations [14] [15]. The modern vector calculus formalism of Maxwell's equations is as follows [16]:

$$\nabla \cdot \mathbf{E} = \frac{1}{\epsilon_0} \rho \quad (\text{Gauss's law}), \quad (2.6)$$

$$\nabla \cdot \mathbf{B} = 0 \quad (\text{no name}), \quad (2.7)$$

$$\nabla \times \mathbf{E} = -\frac{\partial \mathbf{B}}{\partial t} \quad (\text{Faraday's law}), \quad (2.8)$$

$$\nabla \times \mathbf{B} = \mu_0 \mathbf{J} + \mu_0 \epsilon_0 \frac{\partial \mathbf{E}}{\partial t} \quad (\text{Ampère's law with Maxwell's correction}). \quad (2.9)$$

The constants appearing in these equations are the permittivity of free space  $\epsilon_0$  and the permeability of free space  $\mu_0$ .  $\rho$  is the charge density and  $\mathbf{J}$  is the current density.  $\mathbf{E}$  and  $\mathbf{B}$  are the electric and the magnetic field vectors, respectively.

These four equations, with the addition of the Lorentz force equation

$$\mathbf{F} = q(\mathbf{E} + \mathbf{v} \times \mathbf{B}), \quad (2.10)$$

contain the entire theory of classical electrodynamics.

Equations (2.7) and (2.8) imply that the electric and magnetic fields can be expressed by a vector and scalar potential as

$$\mathbf{E} = -\frac{\partial}{\partial t} \mathbf{A} - \nabla \phi, \quad (2.11)$$

$$\mathbf{B} = \nabla \times \mathbf{A}. \quad (2.12)$$

Equations (2.11) and (2.12) imply that it is possible to construct several distinct potentials  $\phi, \mathbf{A}$  that will yield the same electric and magnetic fields  $\mathbf{E}$  and  $\mathbf{B}$ . This redundant degree of freedom, which will not change the observable fields, is known as the principle of gauge freedom. The gauge we will use for our calculations is known as the Coulomb gauge, which imposes the following constraint on the vector potential

$$\nabla \cdot \mathbf{A} = 0. \quad (2.13)$$

The quantum theory of electromagnetic fields is known as quantum electrodynamics. It is, however, common to use a semi-classical picture to describe interactions between quantum mechanical atomic or molecular systems and classical electromagnetic fields. For sufficiently strong fields, the number of photons is so great that the classical picture adequately describes the external field. This follows from Bohr's correspondence principle [17].

Starting with classical Euler-Lagrange formalism [12], it is possible to derive the Hamiltonian for a charged particle in an electromagnetic field. It is

$$\hat{H} = \frac{p^2}{2m} + V(\mathbf{r}) - \frac{q\mathbf{A} \cdot \mathbf{p}}{m} + \frac{q^2 A^2}{2m}, \quad (2.14)$$

where  $\hat{H}_0 = \frac{p^2}{2m} + V(\mathbf{r})$  is the Hamiltonian of the particle without the field, and the interaction Hamiltonian is

$$\hat{H}_I = -\frac{q\mathbf{A} \cdot \mathbf{p}}{m} + \frac{q^2 A^2}{2m}. \quad (2.15)$$

In our case, where  $q = -1$ , we get

$$\hat{H} = \hat{H}_0 + \frac{\mathbf{A} \cdot \mathbf{p}}{m} + \frac{A^2}{2m}. \quad (2.16)$$

This is known as the velocity gauge. By invoking the dipole approximation, which involves a zeroth order expansion in the spatial variables of the field, the  $A^2/2$  term can be dropped by the means of a phase transformation. The dipole approximation is valid when the dimensions of the perturbed system is much smaller than the wavelength of the field.

Having introduced the dipole approximation, it is possible to formulate the Hamiltonian differently. We will look at two possibilities. The first is known as the length gauge, in which the Hamiltonian takes the form

$$\hat{H}_L = \hat{H}_0 + \mathbf{r} \cdot \mathbf{E}. \quad (2.17)$$

The other formulation of the Hamiltonian is known as the Kramers-Henneberg frame and is obtained by the following transformation [18, 19]

$$\hat{T}_{KH} = \exp(-i\boldsymbol{\alpha}(t) \cdot \mathbf{p}), \quad (2.18)$$

$$\boldsymbol{\alpha} \equiv -\int_{t_0}^t \mathbf{A}(t') dt', \quad (2.19)$$

so that the Hamiltonian is

$$\hat{H}_{HK} = \frac{p^2}{2m} + V(\mathbf{r} - \boldsymbol{\alpha}) + \frac{A^2}{2m} \quad (2.20)$$

where the  $\frac{A^2}{2m}$  is the same term as in the velocity gauge (2.16).

## 2.2 Example: Soft Coulomb Potential in One Dimension

Solving the TDSE and TISE in 3D is in some cases computationally demanding even for a single particle. To illustrate the preceding theory with a relevant example we will consider a 1D case.

A useful model potential in atomic physics is the soft Coulomb potential. In our specific case it takes the following form

$$V_{SC} = -\frac{1}{\sqrt{x^2 + k}}, \quad (2.21)$$

where  $x$  is the position in atomic units and  $k$  is an adjustable parameter which ensures that the potential does not blow up at  $x = 0$ .

In this section we start by solving the Schrödinger equation for this potential, and then solve it when the system is influenced by an electric field. As previously mentioned the Schrödinger equation is only analytically solvable for very specific problems; this is not one of them.

To solve the problem we first need to represent our wave function as a combination of basis functions, see equation (2.5). Our choice of basis functions is an orthonormal set of sine functions

$$\phi_i = \sqrt{\frac{2}{L}} \sin\left(\frac{i\pi x}{L}\right), \quad i = 1, 2, \dots, k \quad (2.22)$$

$$\int_{-\infty}^{\infty} \phi_j^* \phi_i dx = \delta_{ji} \quad (2.23)$$

where  $\delta_{ji}$  is the Kronecker-delta,

$$\delta_{ij} = \begin{cases} 1 & \text{for } i = j \\ 0 & \text{for } i \neq j \end{cases}. \quad (2.24)$$

Numerical calculations are necessarily finite in space and time. The spatial dimension of the system is limited by a parameter referred to as the box size,  $L$ , which here represents the size of the system in atomic units. Comparing with equation (2.23), in our specific case the upper limit of the integral is chosen as  $\infty \rightarrow L$  and the lower limit as  $-\infty \rightarrow 0$ . For appropriately selected box limits the chosen basis functions are still orthonormal. The size of the matrices used is determined by  $L$  and by a step size  $dx$ .

We want to solve the TISE (2.4) for the potential  $V_{SC}$ . The Hamiltonian for the system is

$$\hat{H} = -\frac{1}{2m} \frac{d^2}{dx^2} - \frac{1}{\sqrt{x^2 + k}}. \quad (2.25)$$

In light of (2.5), the TISE can be written as

$$\left[ -\frac{1}{2m} \frac{d^2}{dx^2} - \frac{1}{\sqrt{x^2 + k}} \right] \sum_{i=0}^k c_i \phi_i = E \sum_{i=0}^k c_i \phi_i. \quad (2.26)$$

To solve the eigenvalue problem we need to change it to a form that a computer can work with. We start by observing that because of the orthonormality of the selected basis functions, the problem can be significantly simplified by multiplying from the left by  $\phi_j^*$  and integrating from 0 to  $L$ .

$$\begin{aligned} \int_0^L \phi_j^* \hat{H} \sum_{i=0}^k c_i \phi_i dx &= \int_0^L \phi_j^* E \sum_{i=0}^k c_i \phi_i dx, \\ \sum_{i=0}^k \int_0^L \phi_j^* \hat{H} \phi_i c_i dx &= E c_j \quad j = 1, 2, 3, \dots, k. \end{aligned} \quad (2.27)$$

and we have  $k$  equations, one for each  $j$ . Writing out the equation, we get

$$\sum_{i=0}^k \int_0^L \sqrt{\frac{2}{L}} \sin\left(\frac{j\pi x}{L}\right) \left[ -\frac{1}{2} \frac{d^2}{dx^2} - \frac{1}{\sqrt{x^2 + k}} \right] \sqrt{\frac{2}{L}} \sin\left(\frac{i\pi x}{L}\right) dx = E c_j. \quad (2.28)$$

For practical reasons, the potential is centered at  $x = L/2$  with the box extending a distance  $L/2$  to either side. Further calculations yield

$$\frac{2}{L} \sum_{i=0}^k \int_0^L \left[ \sin\left(\frac{j\pi x}{L}\right) \frac{1}{2} \left(\frac{i\pi}{L}\right)^2 \sin\left(\frac{i\pi x}{L}\right) - \sin\left(\frac{j\pi x}{L}\right) \frac{1}{\sqrt{x^2 + k}} \sin\left(\frac{i\pi x}{L}\right) \right] dx c_i = E c_j, \quad (2.29)$$

and due to

$$\sum_{i=0}^k \sin\left(\frac{j\pi x}{L}\right) \sin\left(\frac{i\pi x}{L}\right) = \sin^2\left(\frac{j\pi x}{L}\right), \quad (2.30)$$

and

$$\int_0^L \sin^2\left(\frac{j\pi x}{L}\right) dx = \frac{L}{2}, \quad (2.31)$$

after some simplification we arrive at

$$\frac{(j\pi)^2}{2L^2} c_j - \frac{2}{L} \sum_{i=0}^k \int_0^L \sin\left(\frac{j\pi x}{L}\right) \frac{1}{\sqrt{x^2 + k}} \sin\left(\frac{i\pi x}{L}\right) dx c_i = E c_j. \quad (2.32)$$

Defining

$$\mathbf{c} = \begin{pmatrix} c_0 \\ c_1 \\ \vdots \\ c_j \\ \vdots \\ c_k \end{pmatrix}, \quad (2.33)$$

we observe that we have obtained the eigenvalue problem on matrix form

$$\mathcal{H}\mathbf{c} = E\mathbf{c}, \quad (2.34)$$

where the matrix elements are

$$\mathcal{H}_{ij} = \delta_{ji} \frac{(j\pi)^2}{2L^2} - \frac{2}{L} \int_0^L \sin\left(\frac{j\pi x}{L}\right) \frac{1}{\sqrt{x^2 + k}} \sin\left(\frac{i\pi x}{L}\right) dx. \quad (2.35)$$

We solve this eigenvalue problem numerically by diagonalizing the Hamiltonian matrix  $\mathcal{H}$ , obtaining the set of energies  $E_j$  and the set of eigenvectors  $c_j$  corresponding to the desired states of the systems. The construction of the wave functions is accomplished by combining the basis functions  $\phi_i$  and weights  $c_i$  as in (2.5). The mass  $m$  is set to unity.

A selection of the results from these calculations is shown in figures 2.1, 2.2 and 2.3 below. In all calculations we have used a box size  $L = 2000$  a.u. and the wave functions are constructed using  $N = 900$  basis functions. The parameter  $k$  is set to  $k = 1.4$ . A pictorial representation of the potential can be seen on all graphs.

Figure 2.1 shows  $|\psi|^2$  versus  $x$  for the three lowest bound states, where  $n = \{1, 2, 3\}$ . The weights of the basis functions for the various eigenfunctions are found through (2.32). Note that only a small section of the entire box  $L = 2000$  a.u. is shown. We observe that the bulk of probability densities lies within the well for these states.

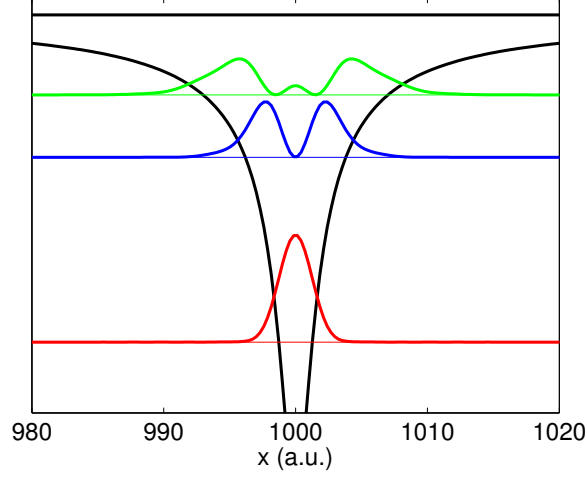


Figure 2.1:  $|\psi|^2$  of the lowest bound states,  $n \in \{1 \text{ (red)}, 2 \text{ (blue)}, 3 \text{ (green)}\}$ , of the soft coulomb potential. Only most relevant range ( $980 \leq x \leq 1020$ ) of the box ( $L = 2000$  a.u.) is shown.

Figure 2.2 shows  $|\psi|^2$  versus  $x$  for states where  $n = \{10, 20, 60\}$ . Out of these three states only the states where  $n = 10$  and  $n = 20$  are bound. We see that as  $n$  increases the states are increasingly spread out in the box.

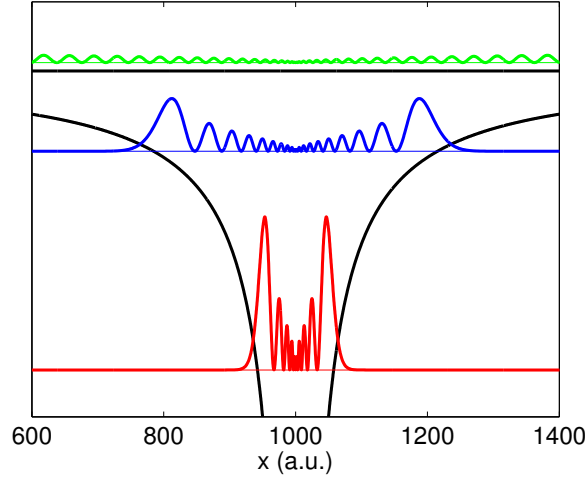


Figure 2.2:  $|\psi|^2$  of the states  $n \in \{10 \text{ (red)}, 20 \text{ (blue)}, 60 \text{ (green)}\}$  of the soft coulomb potential. Range  $600 \leq x \leq 1400$  of total box size ( $L = 2000$  a.u.) is shown. Here only states  $n \in \{10, 20\}$  are bound.

Figure 2.3 shows  $|\psi|^2$  versus  $x$  for the same states as in figure 2.2, under the influence



of a weak field. States  $n = 10$  and  $n = 20$  are shifted slightly towards the left, whereas the state  $n = 60$  has a vanishing probability density for  $x > 1350$  and a diminishing oscillating probability density for  $x < 1350$ .

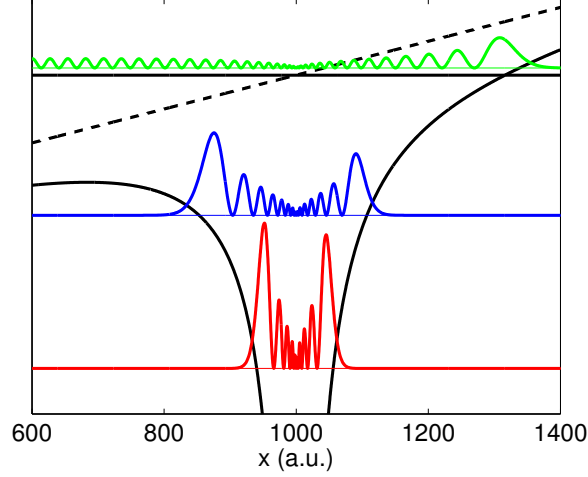


Figure 2.3:  $|\psi|^2$  of the states  $n \in \{10 \text{ (red)}, 20 \text{ (blue)}, 60 \text{ (green)}\}$  of the soft coulomb potential influenced by weak field, where  $E = 10^{-5}$  a.u.. A static electric field,  $E = E_0 \cdot x$ , is applied. Range  $600 \leq x \leq 1400$  of total box size ( $L = 2000$  a.u.) is shown. Here only state  $n = 10$  is bound.

## 2.3 Time Propagation

Out of a manifold of methods to solve the TDSE, two approaches are the most commonly used. The first is the expansion in global eigenstates of the time independent part of the Hamiltonian; the second is the discretization of space and time. The essence of these methods will be shown here.

### 2.3.1 Eigenstate Expansion

Let  $\hat{H}_I(x, t)$  be a time-dependent perturbation (e.g. an electromagnetic field) of a quantum mechanical system. The total hamiltonian operator will in this case be

$$\hat{H}(x, t) = \hat{H}_0(x) + \hat{H}_I(x, t). \quad (2.36)$$

We assume that the stationary states of the unperturbed system are known, they are

$$\Psi_n^0 = \psi_n(x) e^{-iE_n t}. \quad (2.37)$$

We have assumed a one-particle system; the generalization to a many-particle system is straightforward [20]. The time-development of the system is governed by the TDSE (2.1),

$$i\frac{\partial\Psi}{\partial t} = (\hat{H}_0 + \hat{H}_I)\Psi. \quad (2.38)$$

$\hat{H}_I$  is very often an interaction starting at  $t = t_0$  and ending at  $t = T$ ; outside of this time interval it is zero.

The eigenstates of the unperturbed system constitute a complete and orthonormal set, we expand the unknown exact wave function  $\Psi$  in these eigenfunctions  $\Psi_n^0$

$$\Psi(x, t) = \sum_k a_k(t) \psi_k(x) e^{-iE_k t}, \quad (2.39)$$

where the expansion coefficients  $a_k(t)$  will be time-dependent. By defining the following

$$\hat{H}_{I,nk} \equiv \int \psi_n^*(x) \hat{H}_I(x, t) \psi_k(x) d^3x, \quad (2.40)$$

$$\omega_{nk} \equiv E_n - E_k, \quad (2.41)$$

and inserting equation (2.39) in to equation (2.38) and multiplying from the left on both sides of the equation by  $\psi_j(x) e^{-iE_j t}$  and integrating over space it can be shown that

$$\frac{da_n(t)}{dt} = \frac{1}{i} \sum_k \hat{H}_{I,nk} e^{i\omega_{nk} t} a_k(t), \quad (2.42)$$

for  $n = 1, 2, \dots$ . These equations can be written in matrix form as

$$i \frac{d}{dt} \begin{pmatrix} a_1 \\ a_2 \\ a_3 \\ \vdots \end{pmatrix} = \begin{pmatrix} \hat{H}_{I,11} & \hat{H}_{I,12} e^{i\omega_{12} t} & \hat{H}_{I,13} e^{i\omega_{13} t} & \dots \\ \hat{H}_{I,21} e^{i\omega_{21} t} & \hat{H}_{I,22} & \hat{H}_{I,23} e^{i\omega_{23} t} & \dots \\ \hat{H}_{I,31} e^{i\omega_{31} t} & \hat{H}_{I,32} e^{i\omega_{32} t} & \hat{H}_{I,33} & \dots \\ \vdots & \vdots & \vdots & \ddots \end{pmatrix} \begin{pmatrix} a_1 \\ a_2 \\ a_3 \\ \vdots \end{pmatrix}. \quad (2.43)$$

This set of coupled first order differential equations can be solved numerically. In the limit  $k \rightarrow \infty$  the set is completely equivalent to equation (2.38).

### 2.3.2 Discretization

The other common method used to solve the TDSE is the discretization of the wave function in space and time. We consider here the 1D case, and the variables  $x, t$  become

$$x \rightarrow x_i = i\Delta x, \quad (2.44)$$

$$t \rightarrow t_i = i\Delta t, \quad (2.45)$$

where  $i = 1, 2, 3, \dots, n$ . The space- and time derivatives are represented by finite difference schemes [21]. There are numerous method in which to propagate these components; we have chosen the following explicit algorithm [22],

$$\psi(x, t + \Delta t) = \psi(x, t - \Delta t) - 2i\Delta t H(x, t)\psi(x, t). \quad (2.46)$$

We demonstrate the use of this method on the 1D system seen in figure 2.2, where the potential is  $V = 1/\sqrt{x^2 + 1.4}$ . We consider the systems initially in the states  $n = 10$  and  $n = 20$  under the influence of a time-dependent field on the form  $E = E_0 \sin(\omega t)$ . The system is perturbed by a single cycle, where the period is  $T = 1000$  a.u..

Figure 2.4 shows  $|\Psi|^2$  versus  $x$  for the  $n = 10$  state influenced by a pulse with peak field strength  $E_0 = 0.003$  a.u.. The top frame shows the initial state, at  $t = 0$  a.u.. In the next frame, at  $t = 450$  a.u., the wave packet has moved to the left of the potential. In the last frames we see the wave packet spreading out and slowing down as the field shifts direction.

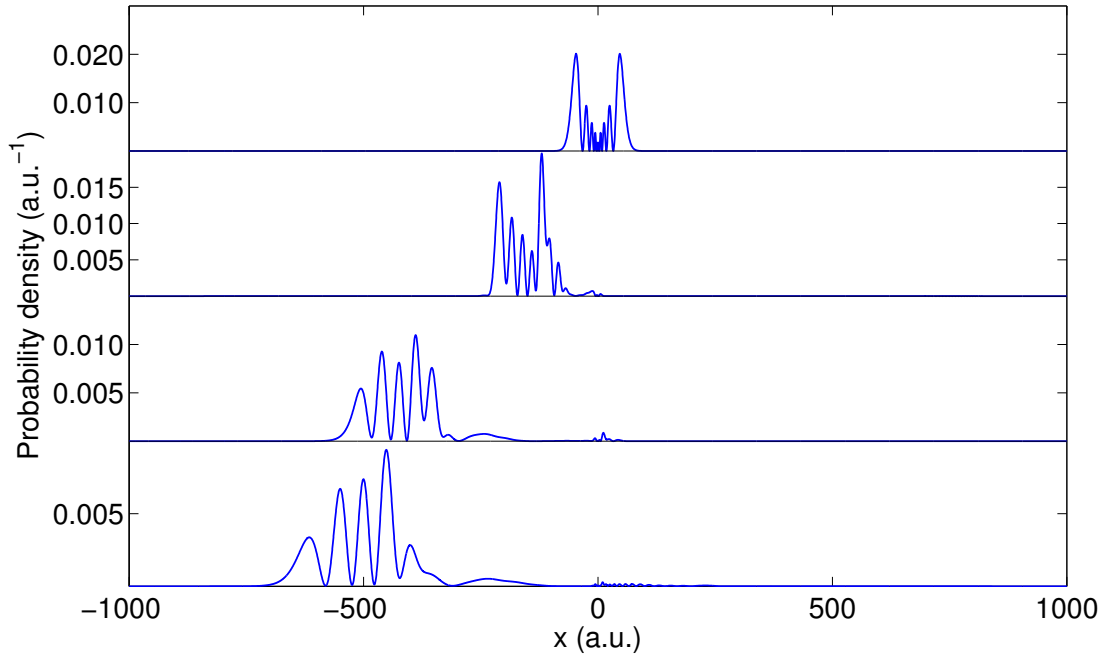


Figure 2.4:  $|\Psi|^2$  versus  $x$  for the  $n = 10$  state of the potential  $V = 1/\sqrt{x^2 + 1.4}$  at various times, influenced by a pulse with peak field strength  $E_0 = 0.003$  a.u.. The unperturbed state can be seen in figure 2.2. The times shown are, in atomic units, from the top:  $t = 0$  a.u.,  $t = 450$  a.u.,  $t = 750$  a.u.,  $t = 1000$  a.u..

Figure 2.5 shows  $|\Psi|^2$  versus  $x$  for the  $n = 20$  state influenced by a pulse with peak

field strength  $E_0 = 0.003$  a.u.. The behaviour of the wave packet is similar to the one in figure 2.4.

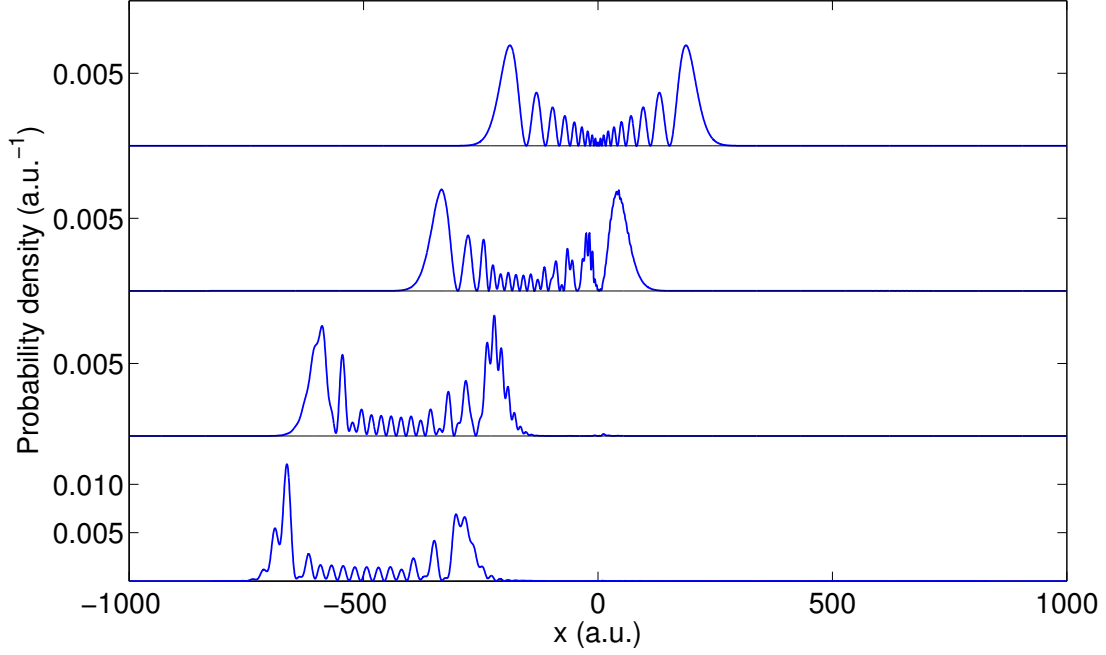


Figure 2.5:  $|\Psi|^2$  versus  $x$  for the  $n = 20$  state of the potential  $V = 1/\sqrt{x^2 + 1.4}$  at various times, influenced by a pulse with peak field strength  $E_0 = 0.003$  a.u.. The unperturbed state can be seen in figure 2.2. The times shown are, in atomic units, from the top:  $t = 0$  a.u.,  $t = 450$  a.u.,  $t = 750$  a.u.,  $t = 1000$  a.u..

Having obtained the wave function numerically at  $\Psi(x, T)$ , where  $T$  is the final propagation time, we can then calculate transition amplitudes. The amplitude for excitation (ionization) to a final level  $\psi_f(x)$  is given by

$$a_f(T) = \int_0^L \psi_f^*(x) \Psi(x, T) dx, \quad (2.47)$$

where  $\psi_f(x)$  is an eigenstate of  $\hat{H}_0$  and  $\Psi(x, t)$  is given by equation (2.39).

The examples of this section are relatively simple. Quantum mechanics gives the most accurate representation of the systems, but 3D quantum mechanical calculations, especially for systems with large spatial or temporal dimensions, are very computationally expensive. Classical methods have the clear advantage of being significantly less expensive. We now shift our focus to the classical trajectory Monte Carlo (CTMC) method.

## Chapter 3

# CTMC - Classical Trajectory Monte Carlo

This section gives an introduction to the techniques used for simulating atomic systems classically. The classical trajectory Monte Carlo (CTMC) method is an extension and special case of a broad class of computational algorithms based on random statistical sampling, known as Monte Carlo methods. The method initially generates a reasonable electronic distribution for the target atom, the microcanonical distribution, which is based on the microcanonical ensemble from statistical mechanics. Reasonable, in this context, means that the properties of the electronic ensemble resemble properties of the corresponding quantum mechanical states. After demonstrating how such a system can be initiated, the scheme for time-propagation of the classical system is presented. We also consider the dynamics of a free electron subjected to an electric field. For a historical introduction to the method, see Chapter 1.

### 3.1 Sampling

#### 3.1.1 Uniform Density Covering of a Disc

Sampling is the essence of the CTMC method. Here we give a short introduction to the sampling techniques used in the present work [23]. We start by considering the relatively simple problem of uniform sampling of points inside a disc of radius  $R$ . A straightforward procedure would be to first distribute the variables  $(x, y)$  over the two regions  $x \in (-r, r)$ ,  $y \in (-r, r)$ , where  $r \geq R$ , and then exclude the points where  $x^2 + y^2 > R^2$ . In this case the integration over all events would have constant density  $\rho(x, y) = k$ ,

$$k \, dx \, dy \rightarrow \rho(x, y) \, dx \, dy. \quad (3.1)$$

A more useful procedure is to use polar coordinates,  $x = r \cos \phi$ ,  $y = r \sin \phi$ , however in this case we must take care in our choice of random variables to ensure a uniform

distribution.

Defining  $rand_1$  as a random number in the interval  $[0, 1]$ , we could naïvely generate variables obeying  $\phi = 2\pi rand_1$  and  $r = R rand_1$ , in which case we would end up with the unwanted nonuniform distribution seen on the left in figure 3.1.

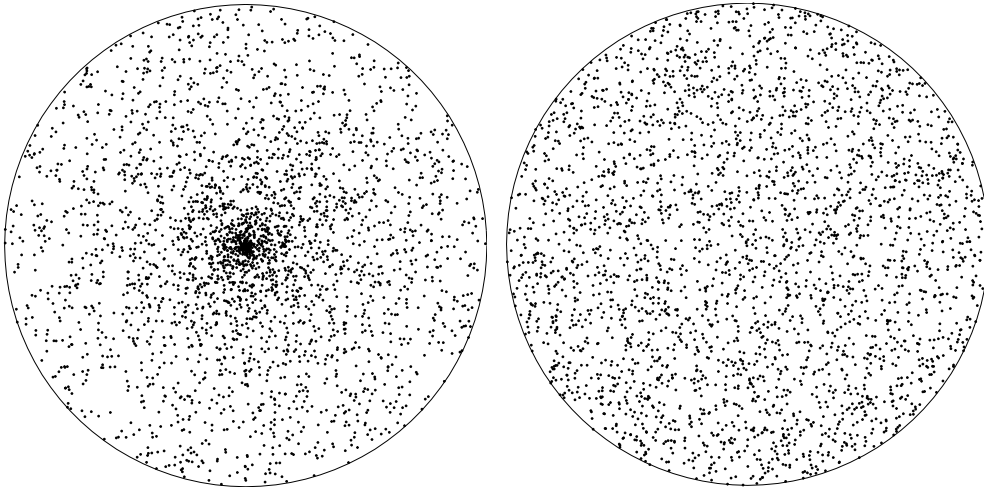


Figure 3.1: Sampling of points inside a disc. Nonuniform sampling using  $r = R rand_1$  seen on the left; uniform sampling using  $r = R\sqrt{rand_1}$  seen on the right.

In order to cover the circle uniformly, we must take as the random variable the probability  $P$  that the point is inside a circle with the given radius  $r$ , inside of the larger circle with radius  $R$ . This probability is given by

$$P = rand_1 = \frac{r^2}{R^2}, \quad (3.2)$$

solving for  $r$  yields

$$r = R\sqrt{rand_1}, \quad (3.3)$$

which gives the desired uniform distribution, as seen on the right in figure 3.1.

In terms of the density discussed above,  $dx dy$  is replaced by

$$r dr d\phi = \rho(r, \phi) dr d\phi, \quad (3.4)$$

where the density  $\rho(r, \phi) = r$  is no longer a constant. Formally, we can introduce a variable  $\omega(r)$

$$\omega = \int_0^r \rho(r') dr' \quad d\omega = \rho(r) dr \quad dr = \frac{d\omega}{\rho(r)}, \quad (3.5)$$

and thus, with  $\omega, \phi$  as new variables

$$\rho(r) dr d\phi = \rho(r) \frac{d\omega}{\rho(r)} d\phi = d\omega d\phi. \quad (3.6)$$

In this case the integral is a very simple function  $\omega(r) = r^2/2$ , which shows that we must choose as  $\omega$  and  $\phi$  as uniformly distributed variables, and setting  $r(\omega) = \sqrt{2\omega}$ , which up to a constant is the same as in equation (3.3). Note that  $r(\omega)$  is the inverse function of  $\omega(r)$  defined by the integral above.

This procedure of obtaining the uniformly distributed variables can be used in general.

The formal procedure is thus as follows: choose two uniformly distributed random numbers  $\omega \in (0, R^2/2)$  and  $\phi \in (0, 2\pi)$  and get the coordinates

$$\begin{aligned} x &= \sqrt{2\omega} \cos \phi, \\ y &= \sqrt{2\omega} \sin \phi. \end{aligned} \quad (3.7)$$

The points  $(x, y)$  are then uniformly distributed inside the disc.

### 3.1.2 Uniform Density Covering of a Sphere

With the spherical coordinates  $r, \theta, \phi$ , where  $r = R$ , the integration over the sphere surface would be

$$\sin \theta_r d\theta d\phi \quad (3.8)$$

so that using  $\theta, \phi$  would require elimination of the  $\rho(\theta) = \sin \theta$ . Also in this case the elementary integral over  $\rho(\theta)$  gives a uniform variable  $t$ , so that

$$\sin \theta_r d\theta d\phi = dt d\phi \quad t = -\cos \theta, \quad (3.9)$$

with  $t \in (-1, 1)$  uniformly distributed. Thus the uniformly distributed variables are  $t$  and the angle  $\phi$ .

This tells us that covering the sphere is just like covering a cylinder of radius  $R$  and height  $2R$  with surface  $2\pi R \times 2R$  by equal portions  $\Delta z$  of the height  $z \in (-R, R)$ , or  $z = Rt$ . Each of the surface elements has a different shape, but all must have the same area, as the constant density indicates.

The formal procedure is thus as follows: choose two uniformly distributed random numbers  $t \in (-1, 1)$  and  $\phi \in (0, 2\pi)$  and get the coordinates

$$\begin{aligned} x &= R\sqrt{1-t^2} \cos \phi, \\ y &= R\sqrt{1-t^2} \sin \phi, \\ z &= Rt. \end{aligned} \quad (3.10)$$

The points  $(x, y, z)$  are then uniformly distributed on the surface of the sphere of radius  $R$  enclosing the origin  $(0, 0, 0)$ .

## 3.2 Initial Conditions

### 3.2.1 The Microcanonical Distribution

We now turn to the appropriate initiation of the atomic system. The initial electronic configuration is generated following Reinhold and Falcón [9]. The approach is based on an analogy of the microcanonical ensemble from statistical mechanics called the microcanonical distribution, where all entities contained in the distribution have exactly specified total energies. In the original paper  $H^+ + He$  and  $H^+ + Li^+$  collisions are considered, however we are concerned exclusively with simulations of systems under the influence of electric fields; this eliminates the need to consider projectiles, thus simplifying the system significantly.

For optimal results the spatial and momentum distribution of the electrons should resemble the quantum mechanical probabilities densities as closely as possible. This is attainable for the momentum distribution, but not the for the spatial distribution. The reason is that for an arbitrarily large momentum, there is a sufficiently small electron orbit radius that would ensure that the system has the appropriate energy. The classical electron does, however, face a limited maximum radius due to its fixed energy, unlike its quantum mechanical counterpart. This limit is reached when  $\mathbf{p} \rightarrow 0$ ; increasing the radius further would violate the condition of fixed energy. The microcanonical distribution in phase space  $(\mathbf{r}, \mathbf{p})$  [6] is

$$\rho(\mathbf{r}, \mathbf{p}) = k\delta(E_i - p^2/2\mu - V(\mathbf{r})), \quad (3.11)$$

where  $k$  is a normalization constant depending on the accessible phase space volume,  $V(\mathbf{r})$  is the effective Coloumb potential,  $\mu$  is the reduced mass of the target core  $M_t$  (*i.e.*  $\mu = M_t/(1 + M_t)$ ) and  $E_i$  is the ionization potential of the active electron. The argument inside the delta function represents the constant energy surface, off of which the probability density must vanish.

The spatial coordinate of the electron is restricted by the relation

$$p^2/2\mu = E_i - V(\mathbf{r}) > 0. \quad (3.12)$$

To determine the possible values of  $r$  we consider the equation

$$E_i - V(\mathbf{r}) = 0 \quad (3.13)$$

and assume for simplicity that it has only one root,  $r_0$ . (3.12) then implies that the values of  $r$  are confined to the single interval  $0 < r < r_0$ .

The method of Reinhold and Falcón transforms the variables  $(\mathbf{r}, \mathbf{p})$  to a set of variables that are uniformly distributed over certain intervals; these variables completely specify the intial state of the system given by the microcanonical distribution (3.11). Note that this method has no real physical justification, it is simply a model. This is clearly seen



when we realize that the electron is placed in a potential  $V(\mathbf{r})$ , which would interfere with the uniform distribution over the phase space  $(\mathbf{r}, \mathbf{p})$ .

In order to work with this distribution we must find the variables which can be uniformly distributed, which is not the case for

$$k\delta(E_i - p^2/2\mu - V(\mathbf{r})) d^3r d^3p. \quad (3.14)$$

which in fact is a five-dimensional space due to the constraint from the  $\delta$ -function. The first step is to recognize that the distribution over the spheres for  $p$  and  $r$  remain unchanged

$$d^3r d^3p \rightarrow r^2 dr d(\cos \theta_r) d\phi_r p^2 d(\cos \theta_p) d\phi_p, \quad (3.15)$$

while the variables  $r$  and  $p$  are not uniformly distributed, and they are further bound to a single variable due to the  $E$   $\delta$ -function. The fact that the unit spheres are covered uniformly is easy to see: the density does not depend anywhere on  $\phi_r$ , so  $\phi_r$  is already uniformly distributed. The total sphere element appears first with a  $\theta$ -dependent density

$$\sin \theta_r d\theta_r d\phi_r, \quad (3.16)$$

but that is quickly removed by

$$\sin \theta_r d\theta_r d\phi_r \rightarrow d(\cos \theta_r) d\phi_r \rightarrow dt_r d\phi_r. \quad (3.17)$$

We must now replace the radial  $p$  and  $r$  by variables  $E$  and  $\omega$ . This must be arranged so that the integration over  $E$  and its  $\delta$ -function can be performed and the  $E$ -dependence eliminated, while the remaining transformed density remains independent of the last new variable  $\omega$ . Since the angles are already described by uniformly distributed  $t_r, \phi_r, t_p, \phi_p$ , we only need to make the transformation

$$p^2 dp r^2 dr \rightarrow dE d\omega. \quad (3.18)$$

Observing that

$$E = \frac{[p(E, r)]^2}{2\mu} + V(r) \iff [p(E, r)]^2 = 2\mu(E - V(r)), \quad (3.19)$$

so that  $p dp \rightarrow \mu dE$  and thus

$$p^2 dp r^2 dr \rightarrow dE \mu p(E, r) r^2 dr = dE \rho(E, r) dr. \quad (3.20)$$

Now the variable  $r$  must be replaced by a new variable  $\omega$ . This is done by defining

$$\omega(r) = \int_0^r \mu p(E, r') r'^2 dr' = \int_0^r \rho(E, r') dr'. \quad (3.21)$$

Note that

$$p(E_i, r) = \sqrt{2\mu(E_i - V(r))}, \quad (3.22)$$

which also limits the values of  $r$  to the interval  $r \in (0, r_0)$ , where  $r_0$  is obtained from

$$E - V(r_0) = 0$$

so that the variable  $\omega$  is limited to  $\omega \in (0, \omega(r_0))$ .

The procedure for obtaining the microcanonical distribution starts by finding the values of  $r_0$  and  $\omega(r_0)$ . After obtaining these, select at random the five variables

$$\phi_r \in (0, 2\pi) \quad t_r \in (-1, 1) \quad (3.23)$$

belongs to the  $r$ -sphere

$$\phi_p(0, 2\pi) \quad t_p \in (-1, 1) \quad (3.24)$$

belongs to the  $p$ -sphere and

$$\omega \in (0, \omega(r_0)). \quad (3.25)$$

The physical coordinates and momenta are then

$$x = r(\omega) \sqrt{1 - t_r^2} \cos \phi_r \quad (3.26)$$

$$y = r(\omega) \sqrt{1 - t_r^2} \sin \phi_r \quad (3.27)$$

$$z = r(\omega) t_r \quad (3.28)$$

$$p_x = p(E_i, r(\omega)) \sqrt{1 - t_p^2} \cos \phi_p \quad (3.29)$$

$$p_y = p(E_i, r(\omega)) \sqrt{1 - t_p^2} \sin \phi_p \quad (3.30)$$

$$p_z = p(E_i, r(\omega)) t_p \quad (3.31)$$

The inverse function  $r(\omega)$  can be found analytically, or perhaps more practically by interpolation from a numerically calculated table of values.

### 3.2.2 Random Number Generation

To initiate the system we need to generate a large number of values within the intervals in equations (3.23), (3.24) and (3.25). True number generators do exist, for example based on the intrinsic randomness of quantum mechanics [24]. For our purposes we are satisfied with a pseudorandom number generator, but it is vital to avoid errors such as repeated sequences of numbers. To accomplish this we use a random number generator subroutine in FORTRAN 95, see [25]. The number generator is initiated by a seed, and to guarantee unique seeds, and thus unique numbers, they are based on the computer time and date.

### 3.2.3 Comparison

A comparison between the CTMC distribution and the quantum mechanical probability density for  $\mathbf{r}$  and  $\mathbf{p}$  of hydrogen in the ground state can be seen in fig. 3.2 and fig. 3.3, respectively. There aforementioned spatial discrepancy is easily observed; the classical electron encounters an upper bound  $r = r_0 = 2$  a.u. due to its fixed energy.

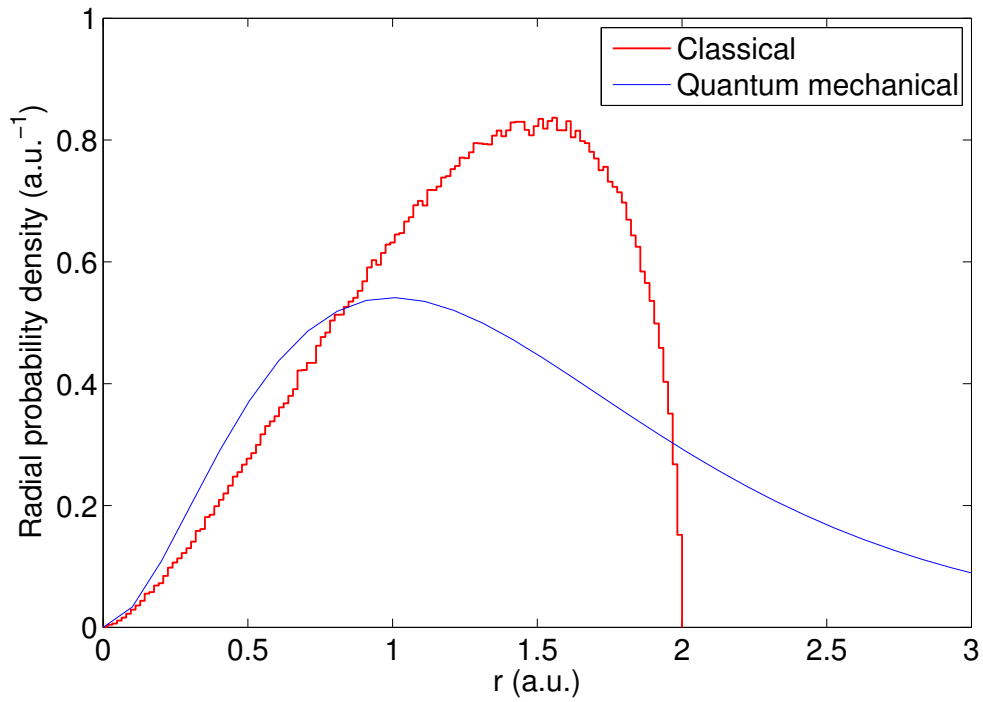


Figure 3.2: Probability density for  $\mathbf{r}$  in H(1s). Microcanonical distribution (red line) and quantum mechanical (blue line).

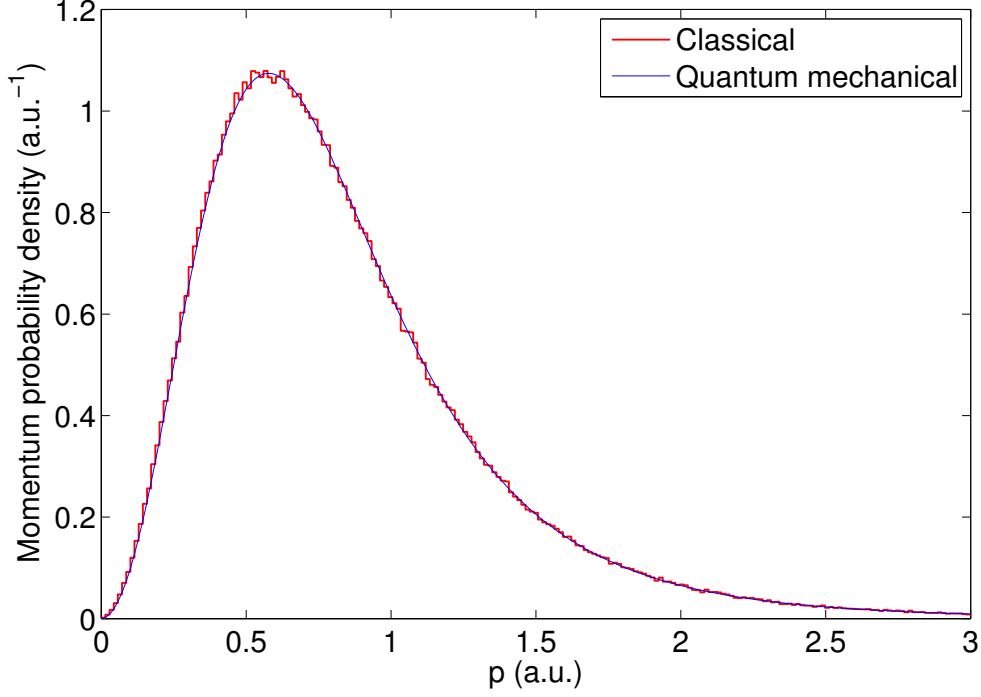


Figure 3.3: Probability density for  $\mathbf{p}$  in H(1s) Microcanonical distribution (red line) and quantum mechanical (blue line).

The distributions shown in figures 3.2 and 3.3 are of H(1s), and some justification for extending the method to higher states and other atoms with a single electron occupying the outer shell (notably Li and Na) is in order. The general character of the momentum distribution for hydrogenic atoms was obtained by Fock in 1935 [26]. He demonstrated that the momentum distribution

$$\rho_n(\mathbf{p}) = \frac{8p_n^5}{\pi^2(p^2 + p_n^2)^4}, \quad (3.32)$$

has the same form for all levels  $n$  of the hydrogen atom, under the condition that the orbital quantum number  $\ell$  states are equally populated. In atomic processes such as scattering and ionization, which we are considering, the momentum distribution plays a crucial role [27]; more so than the position. This implies that we can tolerate an incorrect distribution of positions given a correct distribution of momenta. The angular momenta of our states are distributed, although not evenly, see section 3.2.5. This could potentially lead to less accurate results; we discuss the effect of angular momenta on ionization probabilities in section 4.2.3.

### 3.2.4 Potentials

The electron of the hydrogen atom is subject only to the Coulomb potential  $-1/r$ . We also need to consider the lithium and sodium atoms, which in their neutral states possess 3 and 11 electrons, respectively. Common for all the atoms we consider is that they have a single electron in their outermost shell. Calculating the dynamics of all the electrons simultaneously is a highly demanding numerical task; work in this area is ongoing [28, 29, 30]. The typical approximative approach for such scenarii is to consider only a reduced number of the electrons present - in our case just one, referred to as the active electron. The inactive electrons are only considered as contributors to the potential governing the dynamics of the active electrons. For lithium and sodium the potentials are [31]:

$$V_{Li}(r) = -\frac{1}{r}(1 + (2 + 3.31174r)e^{-3.3117r}), \quad (3.33)$$

$$V_{Na}(r) = -\frac{1}{r}(1 + (10 + 17.9635r)e^{-3.5927r}). \quad (3.34)$$

These potentials have some notable characteristics. As  $r$  grows large the exponential factors become very small, and the potentials become  $V(r) \approx -\frac{1}{r}$ . For smaller distances, the  $r$  factor vanishes and the potentials become  $V_{Li}(r) \approx -\frac{3}{r}$  and  $V_{Na}(r) \approx -\frac{11}{r}$ . The parameters of the equations are chosen so as to give the correct energy levels of the relevant atoms.

### 3.2.5 Angular Momentum

An important property of the ensemble of particles generated for the Monte Carlo method is the distribution of the angular momentum. For most simulations we use the distribution of angular momentum (see figure 3.4) that is generated by the method outlined in section 3.2.1, however for others we only want to consider particles with a specific angular momentum. These are obtained by generating the ensemble in the standard way and picking out the states with the desired angular momentum.

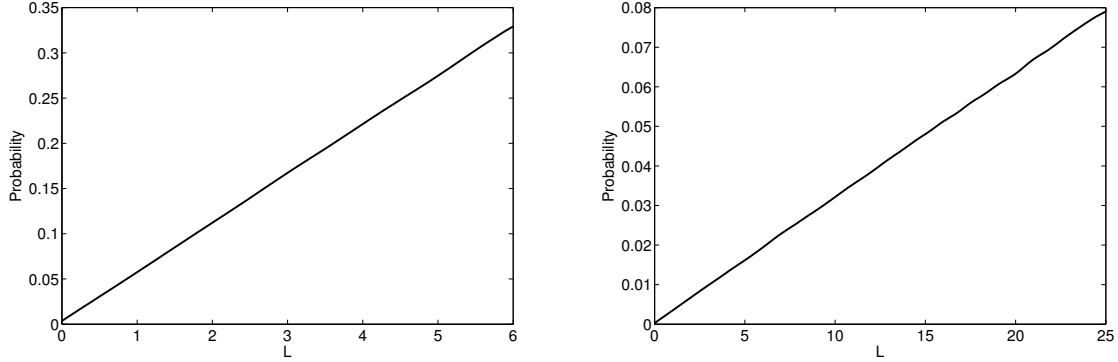


Figure 3.4: Angular momenta  $L$  of the microcanonical distribution. The distributions for hydrogen in the  $n = 6$  state and sodium in the  $n = 25$  state are shown on the left and on the right, respectively. The general shape of the distribution is the same for all relevant elements and states.

The task of picking out the appropriate range of angular momentum to represent a certain quantum orbital angular momentum is not trivial, and can be done in several ways. In quantum mechanics the orbital angular momentum is quantized, with possible values given by  $L_\ell = \sqrt{\ell(\ell+1)}$ , where  $\ell = 0, 1, 2, \dots$ . The first four possibilities are  $L_0 = 0$ ,  $L_1 = \sqrt{2}$ ,  $L_2 = \sqrt{6}$ ,  $L_3 = 2\sqrt{2}$ . We are especially interested in the  $\ell = 2$  ( $d$ -state), where  $L_2 = \sqrt{6}$ , to compare our computational results with recent experiments [32] involving sodium in  $nd$  states.

To pick out the desired states from our continuous distribution we have chosen to select all states with an angular momentum lying in the interval  $\left[L_\ell - \frac{L_\ell - L_{\ell-1}}{2}, L_\ell + \frac{L_{\ell+1} - L_\ell}{2}\right]$ , where  $L_\ell$  is the relevant quantum orbital angular momentum. For the  $d$ -state, the interval is  $\left[\sqrt{6} - \frac{\sqrt{6} - \sqrt{2}}{2}, \sqrt{6} + \frac{2\sqrt{2} - \sqrt{6}}{2}\right]$ .

### 3.2.6 Energies

Obtaining the correct energies for the energy levels of the various atoms is crucial for generating the initial conditions. The energy levels in hydrogen are only dependent on the principal quantum number  $n$  and are readily obtained through

$$E_n = -\frac{1}{2n^2}. \quad (3.35)$$

The energies of alkali atoms can be acquired in a similar manner by introducing a correction known as the quantum defect, which takes into account the fact that nucleus is not entirely screened by the inner electrons. When including the quantum defect, the

energy levels are

$$E(n, l, j) = \frac{1}{2(n - \delta_{nlj})^2}. \quad (3.36)$$

The quantum defect  $\delta_{nlj}$  of a  $nlj$  state is given by

$$\delta_{nlj} = \delta_0 + \frac{\delta_2}{(n - \delta_0)^2} + \frac{\delta_4}{(n - \delta_0)^4} + \frac{\delta_6}{(n - \delta_0)^6} + \frac{\delta_8}{(n - \delta_0)^8} + \dots \quad (3.37)$$

The parameters  $\delta_0, \delta_2, \dots$  can be found in [11]. These parameters are specific to the element and state being considered. We are interested in lithium and sodium in  $nd$  states, for which the parameters can be seen in table 3.1. An overview of the calculated energies for the relevant energy states using these values can be seen in table 3.2.

Element	$\delta_0$	$\delta_2$	$\delta_4$	$\delta_6$
${}^7\text{Li}$	0.002129	-0.01491	0.1759	-0.8507
${}^{23}\text{Na}$	0.015543	0.08535	0.7958	-4.0513

Table 3.1: Quantum defect parameters for Li and Na.

Element	$6d$	$9d$	$12d$	$15d$
H	-0.0138888889	-0.0061728395	-0.0034722222	-0.0022222222
${}^7\text{Li}$	-0.0138973751	-0.0061755428	-0.0034733994	-0.0022228345
${}^{23}\text{Na}$	-0.0139524958	-0.0061929159	-0.0034809109	-0.0022228345

Table 3.2: Energies for certain relevant states

### 3.3 Dynamics

The initial distributions are obtained for a chosen atom (H, Li, Na) and for the preferred energy level  $n$  and angular momentum  $l$ . After obtaining the initial  $(\mathbf{r}, \mathbf{p})$  distribution, simulations are conducted for all generated states. A greater number of simulations ensures a reduction in the statistical error of the calculations.

Our system is governed by classical mechanics, i.e. Newton's laws of motion. We are only interested in the behaviour of the active electron under the influence of an electric field. Calculating the change in coordinates and momentum for the electron is

straightforward, employing the following equations

$$\frac{d\mathbf{r}}{dt} = \frac{d}{dt} \begin{bmatrix} x \\ y \\ z \end{bmatrix} = \begin{bmatrix} p_x \\ p_y \\ p_z \end{bmatrix}, \quad (3.38)$$

$$\frac{d\mathbf{p}}{dt} = \frac{d}{dt} \begin{bmatrix} p_x \\ p_y \\ p_z \end{bmatrix} = \begin{bmatrix} F_x \\ F_y \\ F_z \end{bmatrix}, \quad (3.39)$$

where  $\mathbf{F}$  is derived from the Coulomb potential (screened in the case of Li and Na) and the incident field.

The time-propagation of the system starts simultaneously with, and lasts for the duration of, the field. Equations (3.38) and (3.39) are solved numerically by an ordinary differential equation solver. This specific solver uses a modified divided difference form of the Adams predictor-corrector formulas and local extrapolation [33]. The software developed in conjunction with this thesis allows for output of  $(\mathbf{r}, \mathbf{p})$  at any  $t \in (0, T)$ , where  $T$  is the time at which the field ends. Thus the final state of the electron ensemble can be obtained, as well as data for examining dynamic behaviour and ionization mechanisms.

### 3.3.1 Free Electron

We consider the dynamics of a free classical electron located at the origin and with momentum  $\mathbf{p} = \mathbf{0}$ . This electron is subjected only to a force due to a single cycle of a symmetric electric field; coulomb attraction, or other forces, are not present.

The momentum of a free electron in an electric field at a time  $t$  can be calculated by observing that

$$\frac{d\mathbf{p}}{dt} = \mathbf{F}(t) = q\mathbf{E}(t) = -\mathbf{E}(t), \quad (3.40)$$

and using the fact that for a free electron in an electric field we have  $\mathbf{E}(t) = -\frac{d\mathbf{A}(t)}{dt}$ , so that

$$\mathbf{p} = - \int_{t_0}^t \mathbf{E}(t') dt' = \mathbf{A}(t). \quad (3.41)$$

To find the position of the electron we observe that

$$\frac{d\mathbf{r}(t)}{dt} = \mathbf{p}(t) = \mathbf{A}(t), \quad (3.42)$$

so that

$$\mathbf{r}(t) = \int_{t_0}^t \mathbf{A}(t') dt' = \boldsymbol{\alpha}. \quad (3.43)$$



These calculations are compared with simulations in section 4.2.5.

### 3.4 Analysis

Vast amounts of data can be generated by these simulations. Information about the momentum and position of individual particles in a variety of ensembles is analysed and the results are given in chapter 4. The data allows for many possibilities for analysis; to accommodate the scope of the thesis we have narrowed them down to the most pertinent and interesting ones.

The main results from the analysis of the CTMC data are:

- Ionization probabilities versus field strength for various initial states; compared with experimental results
- Ionization threshold behaviour versus initial states; compared with experimental results
- Energy distribution of electrons from ionized states; compared with experimental results
- Expectation values of momentum and spatial distributions for electrons of various ionized states and field strengths as a function of time
- Final state momentum distribution of ionized electrons
- Individual electron trajectories



# Chapter 4

## Results and Discussion

In this chapter the results of the calculations on alkali Rydberg atoms in THz fields are presented. First, an introduction to some recent experimental results by Li et al. [32] is given. These results were part of the motivation for the present work, and certain simulations are compared to these. In our simulations we use a pulse similar to the one used in experiment; some of the pulse dynamics are also introduced in this section. Following this are the results of 3-D CTMC calculations; this wide range of simulations constitute the bulk of this thesis. In this section we present ionization probabilities for sodium atoms in various initial states and compare the results with experiment; having made the relevant comparisons with experiment, we look at ionization probabilities for other alkali elements and for an extended range of initial states  $n$  as well. After this follows calculations on the ionization probability of alkali elements in initial states with various angular momentum  $\ell$  and energy level  $n$ . Finally, calculations involving energies and dynamics of electrons are presented. These include energy distribution of escaped electrons, spatial and momentum expectation values as a function of time, final state momentum distribution and finally single electron trajectories. Calculations and results similar to those found in this thesis can be seen in the work of Yang et al. [34, 35]. Atomic units (a.u.) used throughout the chapter.

### 4.1 Experiment

The desire to compare computational results with certain experimental results was part of the motivation for the thesis. The experimental results referred to were recently published in a paper by Li et al [32]; they give the ionization probabilities of sodium atoms exposed to intense, single-cycle THz pulses. The atoms are initially in Rydberg states with a principal quantum number in the range  $n \in [6, 15]$  and with a azimuthal quantum number  $l = 2$ , *i.e.* a  $nd$  state.

In short, the authors used two dye lasers to sequentially excite the ground state

sodium atoms to  $nd$  Rydberg states via the intermediate  $3p_{1/2}$  state. The single-cycle THz pulse reaches the sodium atoms  $\sim 20ns$  after they have been excited to the  $nd$  states. The large dimensions of the THz beam ( $\approx 2mm$ ) ensures that the field is uniform over the relevant atoms. Ionization probability versus the maximum field strength  $F_{max}$  of a given field is found by comparing the number of detected electrons or  $Na^+$  ions to the corresponding  $F_{max}$ . We start by looking at the properties of this pulse.

#### 4.1.1 Pulse

An intense single-cycle THz pulse was used to ionize excited atoms. The THz field appears as a single-cycle sine waveform, with a distinct amplitude asymmetry between the negative and positive half cycles. Figure 4.1 and the corresponding caption is taken from their paper and shows a) the maximum momentum transfer and b) the waveform of the field.

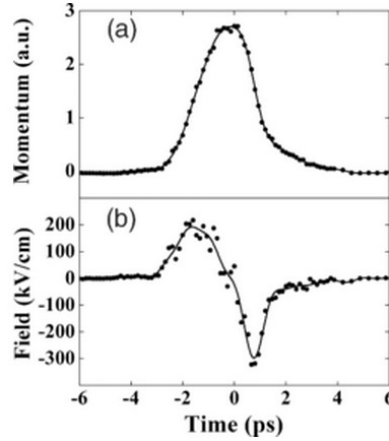


Figure 4.1: a) Maximum momentum transfer from a THz field to low-energy photoelectrons as a function of delay between the electron emission and the temporal center of the THz pulse (points) and FFT filtered data (solid line). b) Single-cycle THz waveform derived from raw data (points) and smoothed data (solid line) in (a). The variation of the data points about the smooth curve reflected the statistical uncertainty which is 10% near the extrema. (Reprint from [34])

The experimental pulse used has the following characteristics:

- Peak field strength up to  $E_0 \approx 430 \text{ kV/cm}$  ( $\sim 10^{12} \text{ W/m}^2$ ;  $\sim 10^{-4}$  a.u.)
- Angular frequency  $\omega = 0.2 \text{ THz}$
- Period  $T \approx 5 \text{ ps}$  ( $\sim 2 \cdot 10^5$  a.u.)

We have used two THz fields in our calculations; one ideal sine wave and one lopsided sine wave similar to the one seen in fig. 4.1. The shape of the THz field has a pronounced effect on the ionization probability, as will be shown later in this chapter. The single-cycle pulses used in our calculations are on the form

$$E = E_0 \cdot \sin(\omega t) \quad (4.1)$$

Characteristics of the pulse used in the simulations depends on the pulse-symmetry. For both symmetric and asymmetric pulses the peak field strength used in our calculations is  $E_0 \approx 1000 \text{ kV/cm}$  ( $\sim 10^{12} \text{ W/m}^2$ ). The asymmetric pulse has the same angular frequency  $\omega$  and period  $T$  as the experimental pulse, whereas the symmetric pulse has the following parameters:

- Angular frequency  $\omega = 1.67 \text{ THz}$
- Period  $T = 6 \text{ ps}$  ( $\sim 2 \cdot 10^5 \text{ a.u.}$ )

In all simulations the dipole approximation has been applied. This approximation rests on the assumption that the spatial dimensions of the system being influenced are small relative to the dimensions of the incident field. When this criteria is met, the field can be assumed to only depend on time, *i.e.*  $E(\mathbf{r}, t) = E(t)$ .

### 4.1.2 Experimental Results

There are two experimental results of interest to us. The first is the ionization probabilities of sodium atoms in a  $nd$  state, where  $n \in [6, 15]$ , versus the peak field intensity  $F_{max}$ , where  $0 \leq F_{max} \leq 430 \text{ kV/cm}$ . From this we can also extract the threshold ionization versus the initial principal quantum number  $n$ ; this threshold ionization field strength  $F_{10\%}$  is defined as the peak THz field required to achieve a 10% ionization probability of the relevant state. The second result we are interested in is the energy distribution of the electrons from ionized states.

We start by showing the ionization probabilities as a function of the peak field strength of the pulse. The original version of the graph, from which the data is taken, can be found in their paper [34].

The ionization probabilities of the various  $nd$  states can be seen in figure 4.2. For certain aspects of the data this is possibly a more informative perspective than the one used in the original paper [32]. The peak field values of each curve have been scaled by  $(n/15)^3$ . The point on the x-axis for which the relevant state starts exhibiting non-zero ionization probability has been moved to  $E = 0 \text{ kV/cm}$ . Displaying the curves in this fashion reveals that the ionization probability varies with the field strength in the same manner for all curves, given the  $(n/15)^3$  scaling.

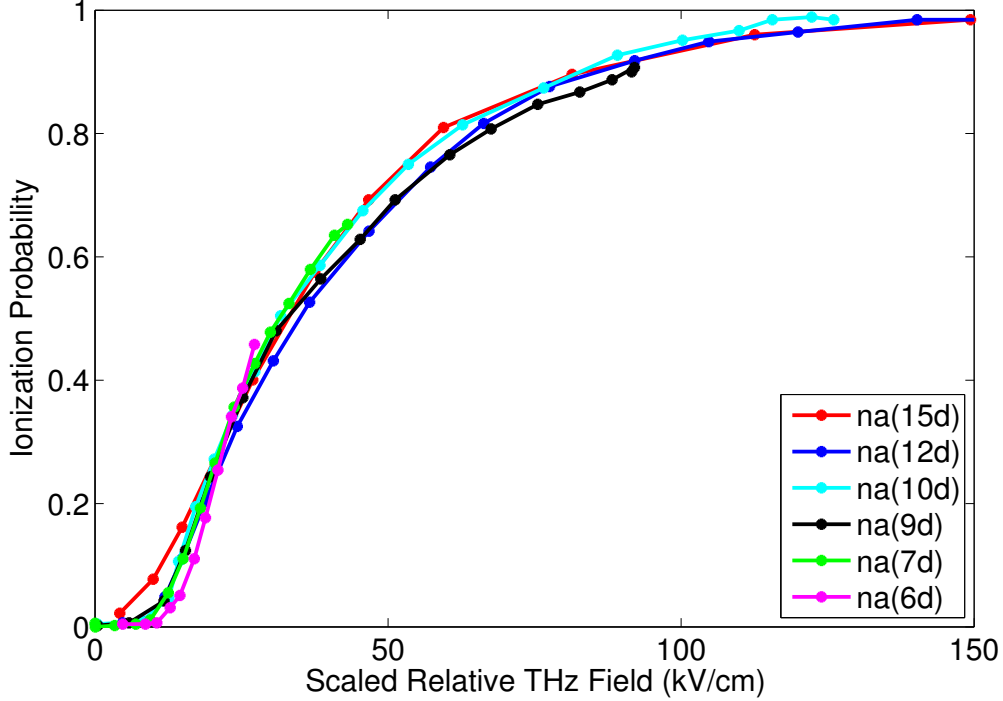


Figure 4.2: Experimental ionization probabilities scaled by  $(n/15)^3$ , stretched and superimposed [36]. Values on x-axis indicates the scaled field strength relative to the lowest point where the ionization probability for the relevant curve is nonzero.

In the relevant range of states,  $n \in [6, 15]$ , states with relatively high initial  $n$  will ionize for lower  $F_{max}$  than states with a relatively low initial  $n$ . Let  $F_0$  denote the threshold between the  $F_{max}$  for which an atom will have a zero chance of ionization and the lowest  $F_{max}$  for which an identically prepared atom will exhibit a non-zero ionization probability. For states with higher initial  $n$  the ionization probability will increase rapidly as  $F_{max}$  increases beyond  $F_0$ ; whereas for states with lower initial  $n$  the ionization probability will increase relatively slowly as  $F_{max}$  increases beyond  $F_0$ . We compare 3D CTMC calculations to these results in section 4.2.1.

The peak field  $F_{10\%}$  versus initial  $n$  is shown in figure 4.3, where logarithmic scales are used on both the horizontal and the vertical axes. Both the figure and the captions are taken directly from the paper. The best fit (dotted line) of the data (filled circles) shows that  $F_{10\%}$  exhibits  $\sim n^{-3}$  scaling behaviour. The authors have also run CTMC calculations which are in somewhat agreement with the experimental results; we compare and discuss the results with our own 3D CTMC calculations in section 4.2.1. As mentioned in their paper, the threshold field for the atoms in the  $nd$  state is higher than expected for adiabatic over-the-barrier ionization, for which it scales like  $n^{-4}$ . Because

of the large electron orbit of the Rydberg states the core scattering effect is suppressed; without the contribution of this mechanism the overall ionization probability decreases.

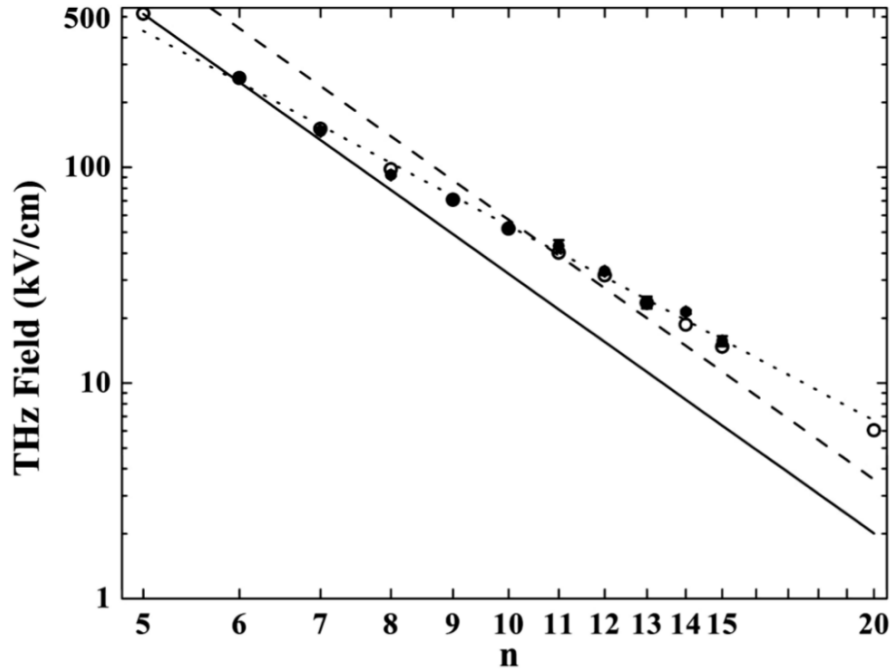


Figure 4.3: Peak THz field required for 10% ionization as a function of  $n$ . (filled circle) Experimental data; (open circle) CTMC calculation; (dotted line) best fit,  $n^{-3}/96$  to experimental data; predicted adiabatic ionization thresholds  $\mathcal{F}_0 = n^{-4}/9$  (dashed line) and  $\mathcal{F}_0 = n^{-4}/16$  (solid line) for hydrogenic and nonhydrogenic Rydberg atoms, respectively. The experimental fields have been scaled by  $1.05x$  to obtain the best agreement with the calculation. Experimental error bars are comparable to the size of the data symbols and are not visible for all points. (Reprint from [34])

In figure 4.4 we see the energy distribution of electrons of the ionized states. Figure and caption are taken directly from paper. The electrons from ionized states with a relatively high initial  $n$  have lower energy than the electrons from states with a relatively low initial  $n$ . Energy distributions from 3-D CTMC calculations and a discussion of the results can be found in section 4.2.4.

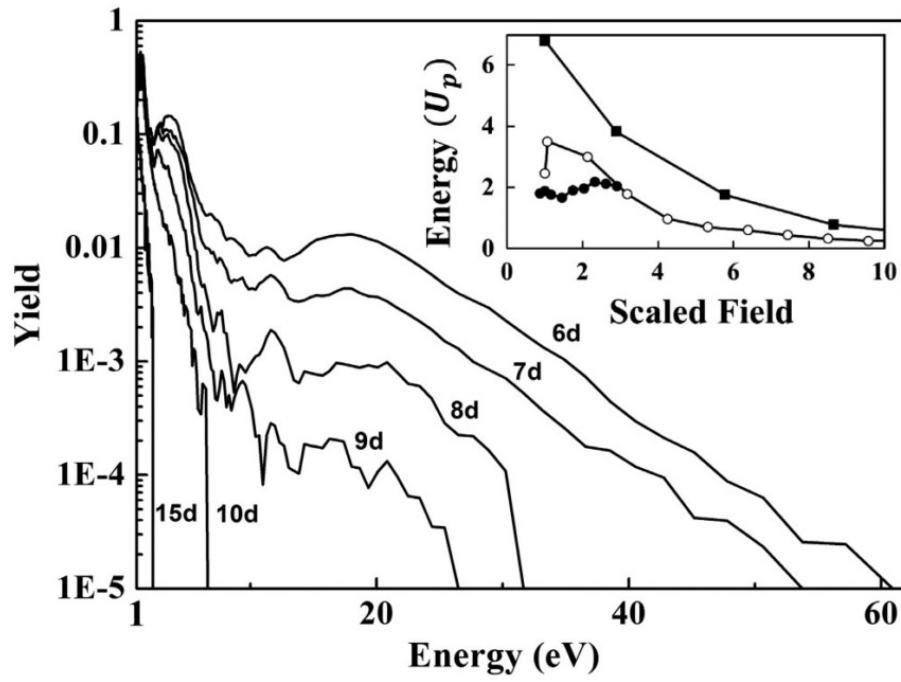


Figure 4.4: Electron energy distributions (energy-integrated yields normalized to 1) for different  $n$  states ionized by a 430 kV/cm single-cycle THz field. Inset: maximum electron energy as a function of  $F_{max}$  for representative states,  $n = 7$  (filled circle),  $n = 11$  (open circle), and  $n = 15$  (filled square). Error bars are smaller than the data symbols. (Reprint from [34])



## 4.2 CTMC - 3D

This section presents the main results of the 3D CTMC calculations. It contains a combination of simulations done on model hydrogen, lithium and sodium atoms with symmetric or asymmetric pulses (see chapter 2) for a range of initial states and field strengths. For a given set of parameters the calculated quantities are based on the aggregated results of simulations of between  $10^4$  and  $10^6$  unique initial conditions, depending on the convergence limit for the particular calculation. Unless specified otherwise, the angular momentum of the electrons used in the calculations of this section have a general angular momentum distribution as seen in section 3.2.5.

### 4.2.1 Ionization Probabilities; Simulations versus Experiment

In this section computational results are compared with experiment. We show the calculated ionization probabilities of the  $6d$ ,  $9d$ ,  $12d$  and  $15d$  states of sodium under the influence of an asymmetrical pulse. These correspond to the experimental results seen in figure 4.2. After making relevant comparisons of ionization probabilities and threshold behaviour, we look at the ionization probabilities for the same ensembles under the influence of a symmetrical pulse.

Figure 4.5 shows ionization probabilities for sodium in  $nd$  states under the influence of an asymmetric field. The peak field strength have been scaled in the same fashion as figure 4.3. Comparing the calculations with experimental results we observe a reasonable agreement for peak field strengths corresponding to low to intermediate ionization probabilities. At higher field strengths the computational results depart from experiment; the calculations suggests that the ionization probability increases faster with increasing field strength.

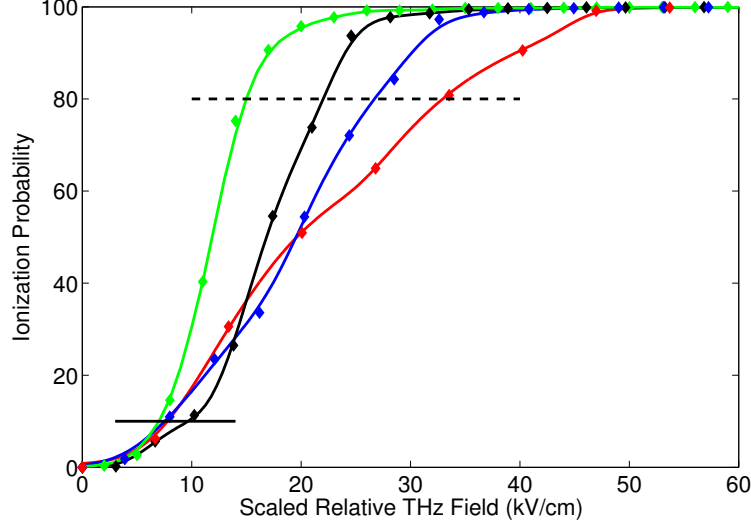


Figure 4.5: Ionization probabilities for sodium atoms as a function of the scaled relative peak field intensity  $F_{max}$  of an asymmetric pulse. Shown is a selection of 4  $nd$  states with the following colors: 15d - green; 12d - black; 9d - blue; 6d - red. Solid lines are fitted to CTMC calculations, shown as diamonds. The solid horizontal line indicates 10% ionization probability; the dashed line indicates 80% ionization probability (see figure 4.6). The peak field strength of the individual curves have been scaled by  $(n/15)^3$ , as in figure 4.3

In figure 4.6 we compare the calculated values for the peak field strengths  $F_{10\%}$  and  $F_{80\%}$  required for a 10% and 80% ionization probability, respectively, as a function of  $n$ . Calculations are fairly successful in reproducing the experimental trend, *i.e.* the  $\sim n^{-3}$  dependence of the 10% threshold ionization. For the 80% ionization threshold the calculations are not in agreement with experiment. In addition to the considerable scaling difference, the experimental results still exhibit  $\sim n^{-3}$  dependence, whereas the corresponding CTMC calculations now show a  $\sim n^{-4}$  dependence.

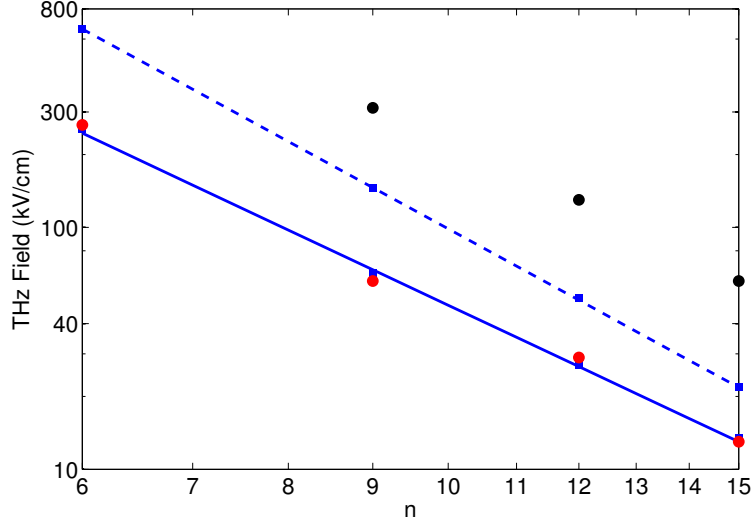


Figure 4.6: Required field strength for 10% (solid line) and 80% (dashed line) ionization probability versus initial  $n$  of the state. CTMC calculations shown in blue, experimental values for 10% shown as red points and experimental values for 80% shown as black points.

The  $n^{-4}$  scaling behaviour observed for the classical calculations at high ionization probabilities is indicative of classical over-the-barrier ionization. The  $n^{-3}$  scaling for lower ionization probabilities is not fully understood, but core scattering effects may be a contributing factor.

For comparison we also consider the ionization probability of sodium under the influence of a symmetric pulse. Figure 4.7 shows the ionization probabilities for sodium in  $nd$  states under the influence of a symmetric field.

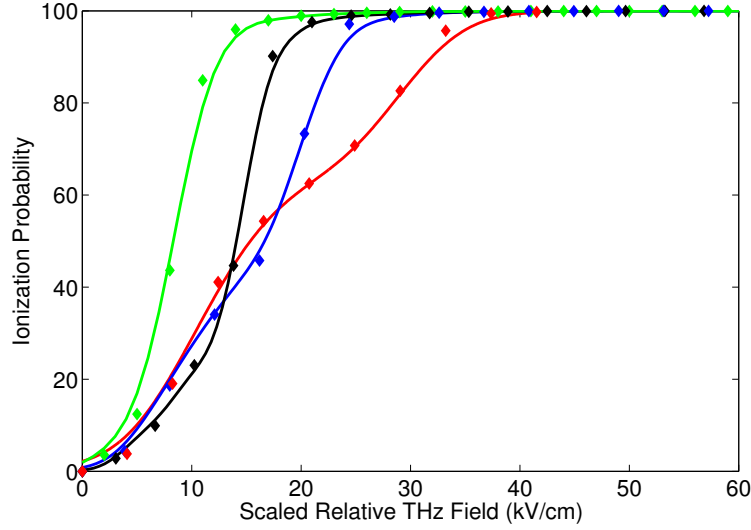


Figure 4.7: Ionization probabilities for sodium atoms as a function of the scaled relative peak field intensity  $F_{max}$  of an symmetric pulse. Shown is a selection of 4  $nd$  states with the following colors: 15d - green; 12d - black; 9d - blue; 6d - red. Solid lines are fitted to CTMC calculations, shown as diamonds. The peak field strength of the individual curves have been scaled by  $(n/15)^3$ , as in figure 4.3

These results are fairly similar to the ones seen in figure 4.5 where the asymmetric pulse was used. The main difference between the two figures is the slightly steeper slope of the ionization probabilities for atoms influenced by the symmetric pulse shape.

### 4.2.2 Ionization Probability Landscapes

Comprehensive simulations were performed on all three elements for a significantly expanded range of initial states,  $n \in [6, 300]$ , with a peak field intensity  $F_{max}$  of up to 500 kV/cm. Both symmetric and asymmetric pulses are used. The results are shown in the following shaded surface plots; ionization probability is indicated by shading as seen on the colorbar in figure 4.8, which shows ionization probabilities for hydrogen atoms initially in a state where  $n \in [6, 25]$  under the influence of a symmetric pulse with a peak field up to  $E = 80$  kV/cm. .

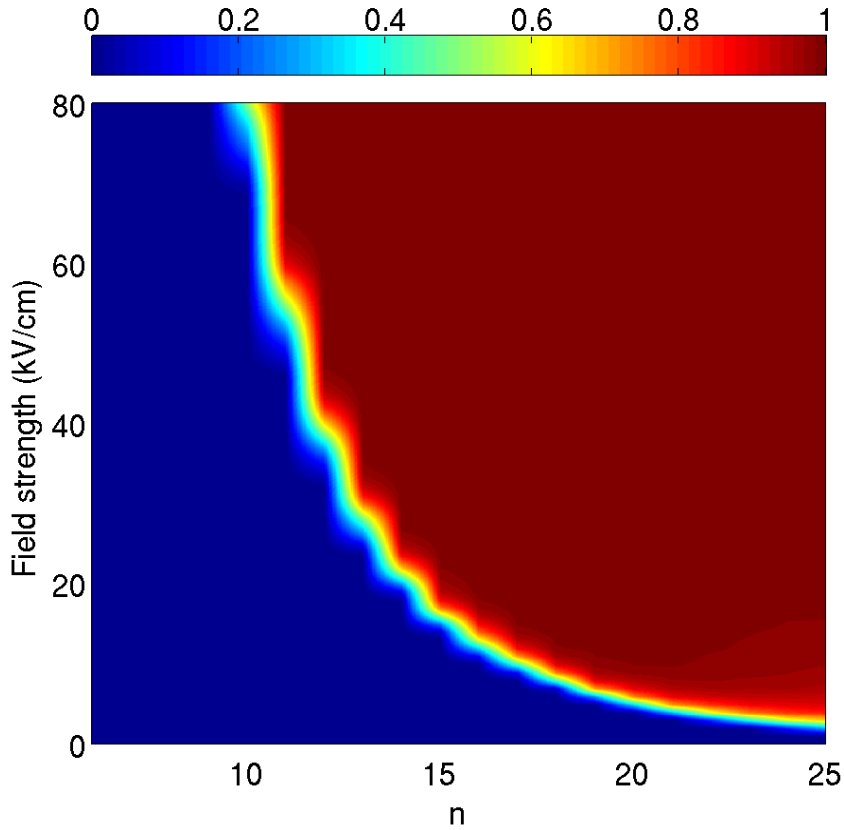


Figure 4.8: Shaded surface plot for the dependence of the ionization probabilities on the peak field strength for hydrogen atoms under the influence of a symmetric pulse. Relatively low-lying states, *i.e.*  $6 < n < 25$ . Color bar above the landscape indicates the values of ionization probabilities; this color convention applies to all subsequent landscapes of the current section.

The ionization probability increases rapidly with increasing  $n$ . This is in contrast

with the behaviour for states with a relatively high initial  $n$ , *i.e.* where  $n > 30$ . This can be seen in the next figure 4.9, which shows ionization probabilities for hydrogen atoms initially in a state where  $n \in [30, 300]$  under the influence of a symmetric pulse with a peak field up to  $E = 500$  kV/cm.

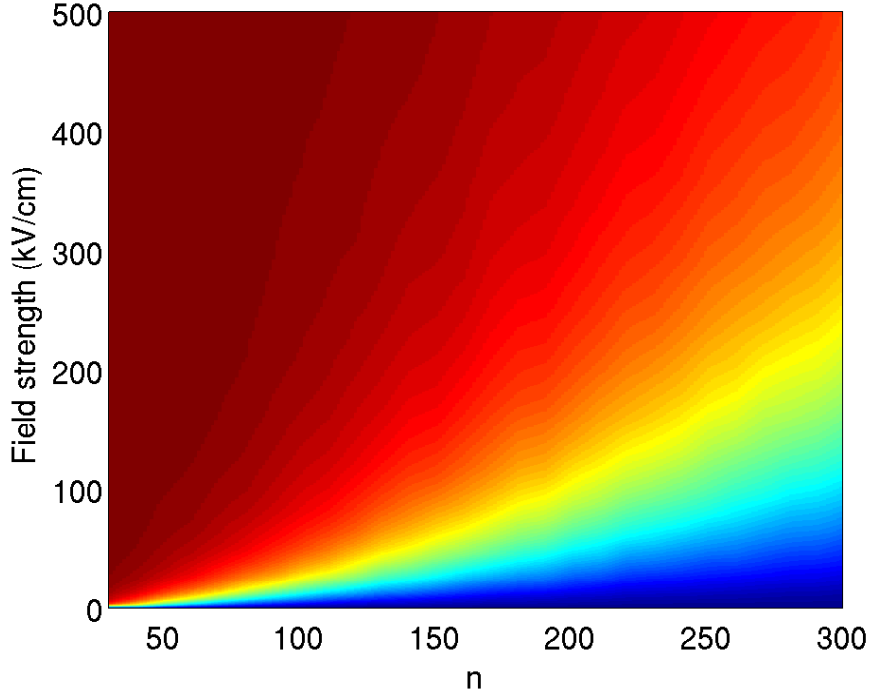


Figure 4.9: Shaded surface plot for the dependence of the ionization probabilities on the peak field strength for hydrogen atoms under the influence of a symmetric pulse. High  $n$  states, *i.e.*  $n > 25$ .

We can clearly see that as  $n$  becomes very large the atoms become increasingly difficult to ionize; the increase is however less abrupt than the corresponding decrease for the low-lying states. This can be understood by considering the extremely large electron orbit ( $r_n \sim n^2$ ) for atoms in high  $n$  states. A large orbit implies a very long period, which for an approximately circular orbit can be adequately expressed by  $T = \frac{2\pi r}{v}$ , where  $r$  is the electron orbit radius and  $v$  is the electron velocity. Due to these large orbits and the relatively short pulse duration, the electron moves approximately in a straight line for the duration of the pulse. The consequence is that the net momentum change  $\Delta p$  is close to zero (more details given in section 4.2.4), and hence the kinetic energy  $E_k$  remains more or less unchanged. The only result of the pulse is an orbital displacement  $\Delta r$ . For a hydrogen atom with total energy  $E_n = -\frac{1}{2n^2}$  and  $r_n = n^2$  the condition for

ionization is  $E_n + \Delta E_p \geq 0$ , where  $E_p = \frac{1}{r}$  is the potential energy. If  $r_n$  is the initial orbit radius and  $\Delta r$  is the displacement we get

$$E_n + \frac{1}{r_n} \geq \frac{1}{r_n + \Delta r} \quad (4.2)$$

which implies that  $\Delta r \geq n^2$  in the event of ionization. Similar calculations were performed, and similar results obtained, by Yang et al [34].

Figure 4.10 show calculations similar to the ones seen in figures 4.8 and 4.9, only with an asymmetrically shaped pulse. A notable difference between the simulations with a symmetric pulse versus the ones with an asymmetric pulse is the difference in the width of the region of intermediate ionization probability; figures where an asymmetric pulse has been used display a narrower region than the ones with a symmetric pulse.

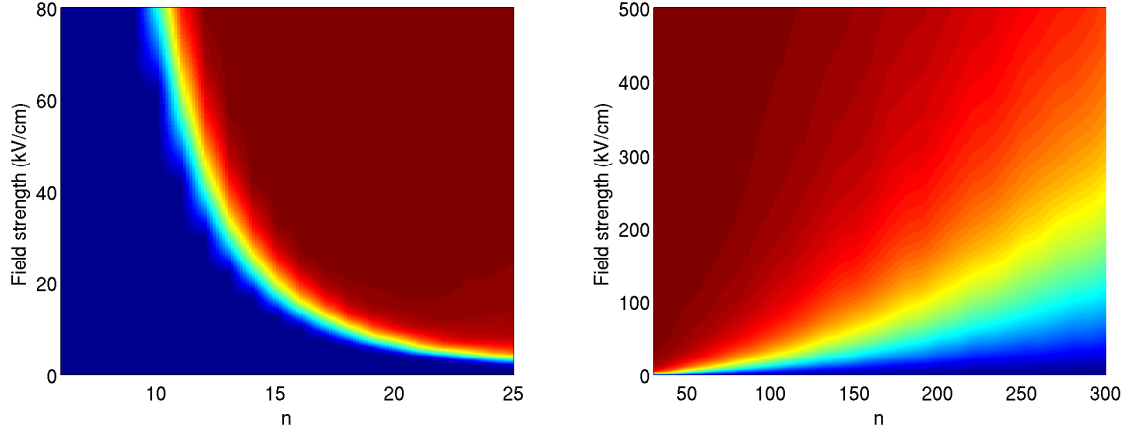


Figure 4.10: Shaded surface plots for the dependence of the ionization probabilities on the peak field strength for hydrogen atoms under the influence of a asymmetric pulse.

Similar calculations were performed for sodium and lithium atoms. The difference in ionization probabilities between the various elements is not very pronounced, especially not for high  $n$ , so these calculations will not be displayed. When the outer electron of the lithium or sodium atom is far away from the nucleus, as is the case with the Rydberg atoms, the core electrons screens the charge of the nucleus. An arbitrary neutral atom with a nucleus with charge  $+Z$  is surrounded by electrons with a combined charge of  $-Z$ . As the outer electron gains energy and increases its orbital radius, the combined charge of the nucleus and the other electrons will be  $Z + (-Z + 1) = +1$ . When the outer electron is sufficiently distanced from the core, this "effective charge" is the charge it experiences. It is the same as the exact charge the electron in the hydrogen atom experiences. This

can also be confirmed by observing that as  $r$  becomes large, the potentials  $V_{Li}$  and  $V_{Na}$  from section 3.2.4 go to  $-\frac{1}{r}$ .

Figure 4.11 shows the peak field strength  $F_{10\%}$  required for 10% ionization probability for hydrogen, lithium and sodium initially in states where  $n \in [6, 300]$  under the influence of both symmetric and asymmetric field.

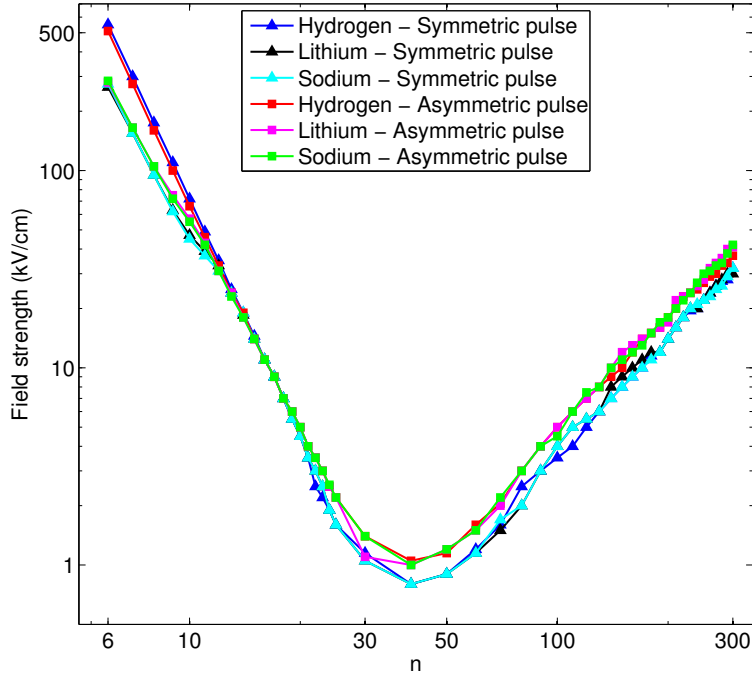


Figure 4.11: Peak field strength required to achieve 10% ionization probability (threshold ionization) for all three elements under the influence of symmetric and asymmetric pulses.

The aforementioned behaviour can be clearly seen in this figure. The general behaviour is similar for all three elements. The minimum threshold ionization required for all elements is found at  $n \approx 40$ ; the required field strength is lower for the symmetric pulse than for the asymmetric pulse. For  $n$  less than  $\approx 40$  the threshold ionization decreases with increasing  $n$  as  $\sim n^{-3}$ , whereas for  $n$  larger than  $\approx 40$  the threshold ionization increases with increasing  $n$  as  $\sim n^2$ . These results suggest that there is a certain range of  $n$ 's where the required field to ionize is low relative to both higher and lower states. These results were also found by Yang et al [34]; they coined the phrase "ionization window" for the states in the proximity of  $n = 40$ .

In this intermediate region the effects of increasingly large electron orbits start to dominate, decreasing ionization probability as  $n$  increases, as explained earlier in the present section.



### 4.2.3 Orbital Angular Momentum

In this section we look closer at ionization probabilities as a function of maximum field strength for states with various angular momentum. There is no classical equivalent of the quantum orbital angular momentum; here we use an appropriate analogue, see section 3.2.5.

The initial angular momentum we have used in the calculations is either  $\ell \in \{2, 3, 4\}$  or a distribution of angular momentum states as seen in the aforementioned section. We wish to investigate what influence the angular momentum of the initial states has on the ionization probability, and we start by examining the case of hydrogen initially in  $n \in \{9, 12, 15\}$  states. The section continues with simulations for lithium and sodium with various initial  $n$ 's and  $\ell$ 's under the influence of both symmetric and asymmetric fields.

Figures 4.12 show the ionization probability of states with various initial  $n$  and  $\ell$ .

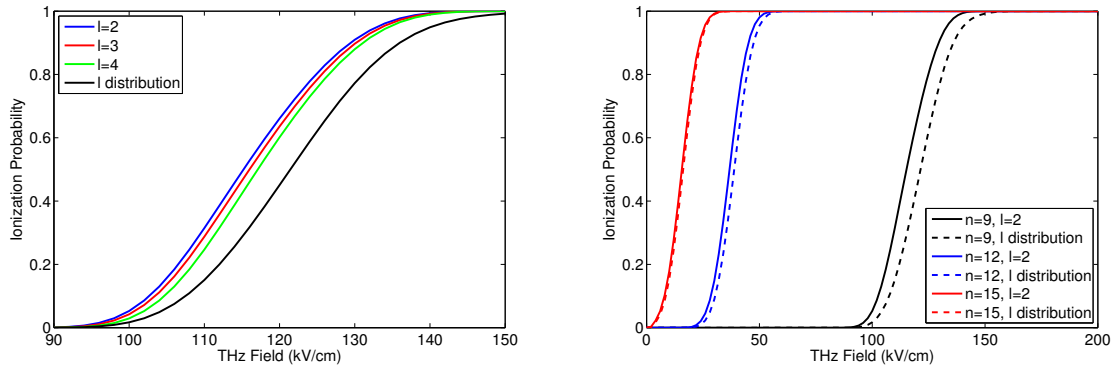


Figure 4.12: Ionization probability versus maximum field strength for hydrogen initially in a  $n = 9$  state seen on the left. Initial angular momenta of electrons in ensemble is either  $\ell \in \{2, 3, 4\}$  or a distribution like the one seen in section 3.2.5. Similar graph for  $n \in \{9, 12, 15\}$  and  $\ell = 2$  or  $\ell$  distributed shown on the right. Symmetric field used in all calculations.

The figure on the left shows that states with low angular momentum ionize before states with a relatively large angular momentum. The ionization probability for ensembles with a distributed angular momentum is consistent with this behaviour; most of the angular momentum in the distribution will be close to the maximum angular momentum  $\ell = n$ . In the figure on the right the ionization probability versus peak field strength for ensembles of states initially in  $n = \{9, 12, 15\}$  with various  $\ell$  is shown. We observe the same behaviour as in the figure on the left, *i.e.* states with relatively low initial  $\ell$  ionizes on average before states with relatively high initial  $\ell$ . The difference in the ionizing behaviour of ensembles consisting of particles with initial angular momentum  $\ell = 2$  and ensembles with a distribution of  $\ell$ 's is less prominent for higher  $n$ . The influence of the

Coulomb attraction from the core on the electron dynamics likely plays an important role in the ionization probabilities of the various states; for states in which the electron has a larger orbiting radius this influence is relatively small. A possible consequence is that the angular momentum, which determines the orbit around the core, is also less influential for the states with relatively high  $n$ .

Figure 4.13 shows that ionization probability for lithium and sodium initially in the  $n = 6$  state and with various angular momenta  $\ell$ . For symmetric and asymmetric pulses we observe again that ensembles consisting of states with a relatively low initial  $\ell$  ionize first. Here, however, the ensemble with distributed  $\ell$  is not the one that ionizes for the lowest peak field strength  $F_{max}$ . There are several possible contributing factors to this. The  $n = 6$  state is low relative to the states considered otherwise in the current subsection, and a substantial amount of the particles in the ensemble with a distribution of angular momentum  $\ell$  will have the same angular momentum as the ensembles consisting purely of states with  $\ell = 2$ ,  $\ell = 3$  or  $\ell = 4$ . Additionally, these are the potentials for sodium and lithium and thus we can expect a different behaviour than for the simple hydrogen  $V = -1/r$  potential used in figures 4.12.

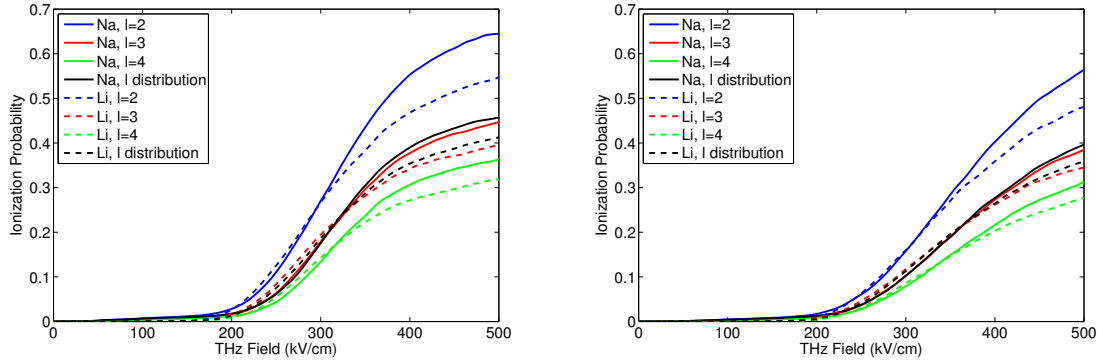


Figure 4.13: Ionization probabilities versus maximum field strength for sodium and lithium initially in a  $n = 6$  state, with various angular momentum  $\ell$ . Symmetric and asymmetric pulses were used on the left and the right, respectively.

There is a visible difference between the ionization probabilities for the symmetric and the asymmetric pulse shape. As seen in section 4.2.1, the ionization probabilities for the symmetric pulse shape are greater. The symmetric pulse shape has the same peak field strength for both half-cycles. The first half-cycle of the asymmetrical pulse has a peak field strength downscaled by a factor of 1.5 relative to the last half-cycle, reducing the probability of the pulse ionizing the atom during the first half-cycle compared to a symmetric pulse shape.

For a relatively high peak field strength the sodium atoms ionize before equivalent

states in lithium atoms. This can be attributed to the potentials used; for a given state - and therefore electron orbit radius - the electrons in lithium are more strongly bound to the nucleus than the ones in sodium.

The ionization probability for sodium and lithium with  $\ell$ -states where  $n = 12$  can be seen in figure 4.14. We see a similar trend as in figure 4.13, however the difference between the various states is less prominent. The difference in ionization probabilities when using the symmetrical versus the asymmetrical pulse shape is smaller here, although the symmetric pulse shape still ionizes the atoms before the asymmetric pulse shape. For small (*i.e.*  $\sim 5\%$ ) and large (*i.e.*  $\sim 95\%$ ) ionization probabilities there is almost no appreciable difference between the states or elements.

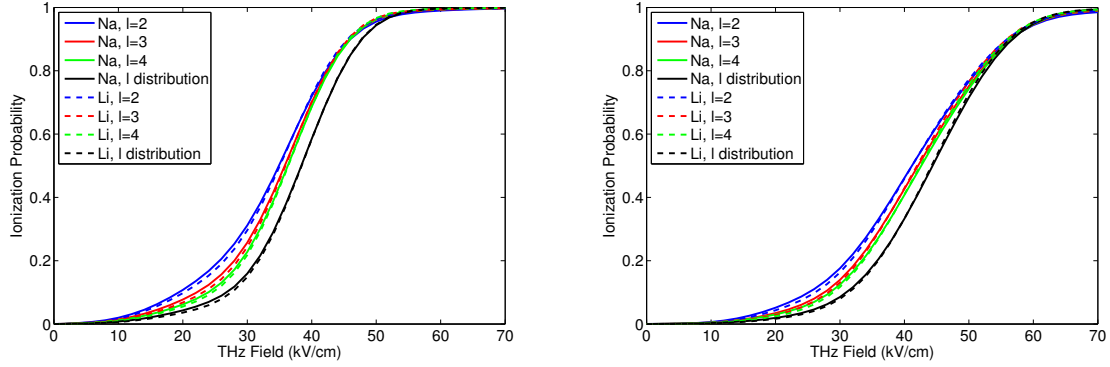


Figure 4.14: Ionization probabilities versus maximum field strength for sodium and lithium initially in a  $n = 12$  state, with various angular momentum  $\ell$ . Symmetric and asymmetric pulses were used on the left and the right, respectively.

#### 4.2.4 Free Electron Energy Distribution

In this section we look at the energy distributions of the electrons with a positive energy, which we regard as having escaped the attractive Coulomb force from the core. We consider hydrogen and sodium atoms initially in a  $n = \{6, 9, 12, 15\}$  state, influenced by either a relatively strong or a relative weak field. The weak field approximately corresponds to the peak field strength required to ionize  $\sim 50\%$  of the relevant states of the element, whereas the strong field corresponds to the peak field strength required to ionize  $\sim 100\%$  of the relevant states. Calculations are shown for both symmetric and asymmetric pulses. All figures feature electrons from ensembles initially with a distributed angular momentum as seen in section 3.2.5, with the exeption of figure 4.15, where  $\ell = 2$ .

In all graphs only the free electrons from ionized atoms are considered. This subset of the total ensemble of particles is renormalized, *i.e.* the energy integral over the whole distribution of free electrons is unity. The x-axis displays energy, in atomic units, and the y-axis displays the probability density  $dP/dE$  [ $eV^{-1}$ ]. The pulse symmetry properties are displayed in the legends.

We start by comparing computational results with experimental results. The energy distribution of the electrons in the experiment can be seen in figure 4.4. The peak field strength of the asymmetric pulse is  $E = 430$  kV/cm. Figure 4.15 shows the energy distribution of electrons from ionized states of sodium under the influence of an asymmetric pulse with peak field strength  $E = 430$  kv/cm; the electrons are initially in states with  $n \in \{6, 9, 12\}$  and  $\ell = 2$ .

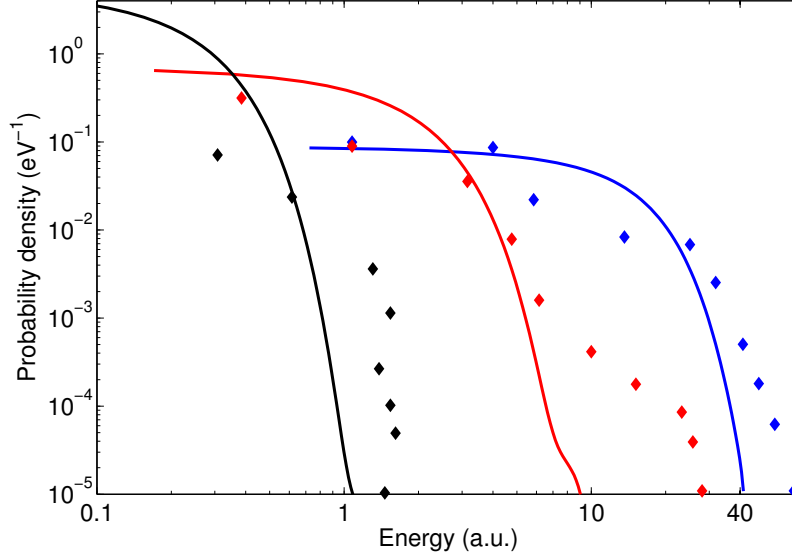


Figure 4.15: Energy distribution of electrons from ionized states of sodium initially in a state with  $n = \{6 \text{ (blue)}, 9 \text{ (red)}, 15 \text{ (black)}\}$  and  $\ell = 2$ . Solid lines are smoothed curves from CTMC calculations, diamonds are data points extracted from experimental values in figure 4.4. The asymmetric pulse used has a peak field strength  $E = 430 \text{ kV/cm}$ .

The figure shows that the more detailed properties of the system are harder to reproduce classically. There is some agreement between the experimental and the calculated data, but clearly there are one or several mechanisms that are not properly reproduced with classical calculations.

We continue this section by considering the energy distribution of electrons from ionized states of hydrogen and sodium, where the pulse has various strength and symmetric properties.

Figure 4.16 shows the energy distribution of electrons from the ionized states of hydrogen and sodium initially in the  $n = 6$  state.

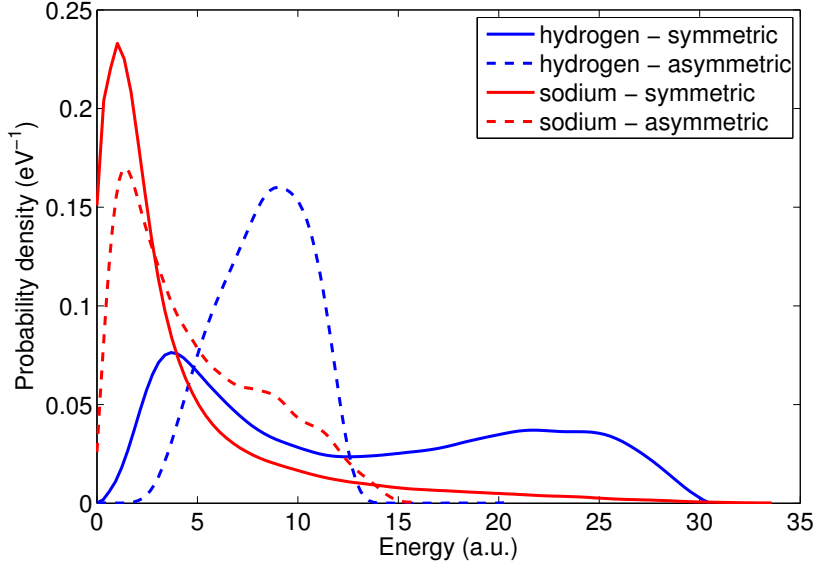


Figure 4.16: Energy distribution of free electrons initially bound in the  $n = 6$  state in hydrogen and sodium atoms.  $dP/dE$  (atomic units) versus electron energy (eV). Incident with a relatively low field strength, ionizing  $\sim 50\%$  of states ( $E = 650$  kV/cm for hydrogen atoms and  $E = 550$  kV/cm for sodium atoms).

We observe that there is a distinct difference in the energy distribution for electrons of both hydrogen and sodium exposed to the symmetric pulse versus those exposed to the asymmetric one. The electrons exposed to the symmetric pulse display a somewhat low variance in energy compared to the ones exposed to the asymmetric pulse. Hydrogen in the  $n = 6$  states exposed to the asymmetric field has the broadest range of energies, fairly evenly distributed in the interval  $E \in [3, 30]$ . The differences between the energy distributions for the two elements is most emphasized for the relatively low lying state  $n = 6$ , as seen by comparing with figures 4.18, 4.19 and 4.20; this can be understood by considering the potentials seen in section 3.2.4. As the orbiting radius  $r$  of the electron increases the potential representing the sodium atom becomes increasingly similar to the hydrogen potential  $V = -\frac{1}{r}$ .

The energy distributions seen in figure 4.17 are of electrons exposed to a field that is strong relative to the one used for the simulations seen in figure 4.16. In the strong symmetric field the probability density is greatest in the region where  $E < 10$ , whereas in the energy distribution from the asymmetric field we observe two peaks in each of the two probability densities.

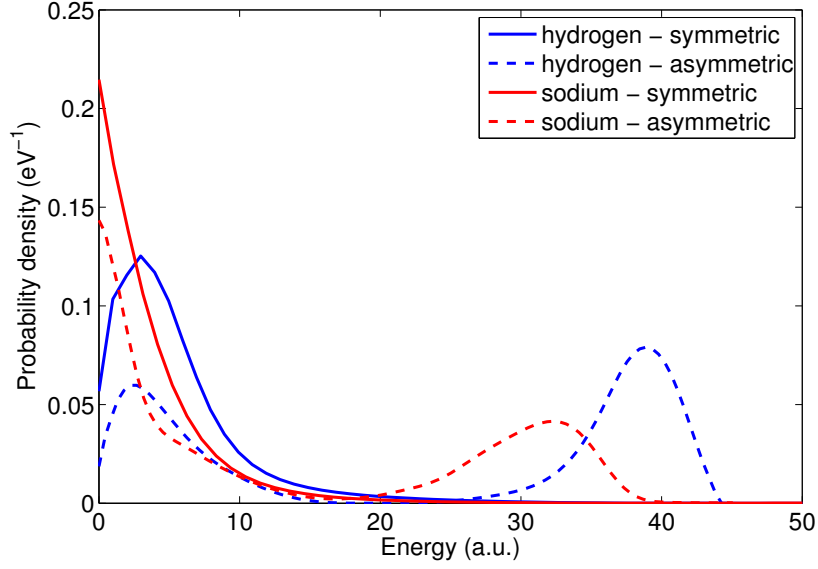


Figure 4.17: Energy distribution of free electrons initially bound in the  $n = 6$  state in hydrogen and sodium atoms.  $dP/dE$  (atomic units) versus electron energy (eV). Incident pulse with a relatively high field strength, ionizing  $\sim 100\%$  of states ( $E = 1000$  kV/cm for hydrogen atoms and  $E = 950$  kV/cm for sodium atoms).

The energy of the freed electrons depend on its momenta, as  $E = p^2/2 - 1/r$ . So the final energy of the electron depends on the momentum transfer from the field to the electron. Following the dipole approximation and assuming a negligible magnetic field, the electron experiences a force  $\mathbf{F} = q\mathbf{E}$ , where  $q = -e$ . During the first half-cycle the field points in the  $+z$  direction, thus the electron will experience a force in the  $-z$  direction; during the second half-cycle the situation is reversed, with the field pointing in the  $-z$  direction and the electron experiencing a force in the  $+z$  direction. As long as the electron is still bound to the core the change in its momentum is small relative to the case for the free electron.

The change in the momentum of the non-bound electron is

$$\frac{d\mathbf{p}}{dt} = \mathbf{F} = q\mathbf{E} = -eE_0 \sin \omega t \quad (4.3)$$

where  $\omega$  is the angular frequency and  $E_0$  is the maximum field strength. The total change in momentum is

$$\Delta\mathbf{p} = -eE_0 \int_{t_{min}}^{t_{max}} \sin \omega t dt = \frac{eE_0}{\omega} \cos \omega t \Big|_{t_{min}}^{t_{max}} \quad (4.4)$$

where  $t_{min}$  and  $t_{max}$  are the times at which the field is switched on and off, respectively. Now, because  $\omega t_{min} = -\pi$  and  $\omega t_{max} = \pi$ , we obtain

$$\Delta \mathbf{p} = \frac{eE_0}{\omega} (\cos(-\pi) - \cos(\pi)) = 0. \quad (4.5)$$

This calculation is for the free electron; the electrons we are considering are initially bound to the core and are only freed at some time  $t_{free}$ . Assuming a negligible momentum transfer from the field to the electrons during the time which they are bound, the total change in momentum due to the field will be

$$\Delta \mathbf{p} = \frac{eE_0}{\omega} \cos \omega t \Big|_{t_{free}}^{t_{max}}. \quad (4.6)$$

The maximum momentum transfers happens at if  $t_{free} = 0$ . This is unlikely to happen, however, due to the field  $E = E_0 \sin \omega t$  vanishing at that particular time. The total momentum will however increase as  $t_{free}$  approaches  $t = 0$  from the left, and decrease as  $t_{free}$  departs  $t = 0$  to the right. This can be used to partly explain the large variations in the energy distributions in this section; core scattering also plays an important role in the shape of the energy distributions in the present section.

In figure 4.17 we see a large probability of finding electrons with low energies. The strong field strength compels the electrons to escape quickly, so that  $t_{free} \approx t_{min}$  and the total momentum transfer, and thus the energy, is low. For the asymmetric field we see additional peaks centered around  $E \sim 32$  a.u. and  $E \sim 39$  a.u. for sodium and hydrogen, respectively. These peaks represent the electrons that were still bound after the first half-cycle, and only manage to break free during the second half-cycle. These electrons will only gain momentum in the  $+z$  direction, and their final energy will be relatively high.

Figure 4.18 shows the energy distributions of the free electrons for sodium and hydrogen atoms initially in a  $n = 9$  state. Compared to the  $n = 6$  case the differences between the elements is smaller. The figure on the left is for the relatively weak field; here the asymmetric pulse yields an energy distribution with a low variance relative to the symmetric case, indicating that the electrons exposed to the symmetric pulse will escape the atom for a broader range of times than those exposed to the asymmetric pulse. For the strong-field case on the right, the differences between the distributions for the elements and the pulse shape symmetry are smaller. The asymmetric pulse still yields peaks in the probability densities at higher energies, indicating that the asymmetric pulse will free the electrons at times where the symmetric pulse will not. The yield of the high-energy peaks is however smaller than for the  $n = 6$  case.



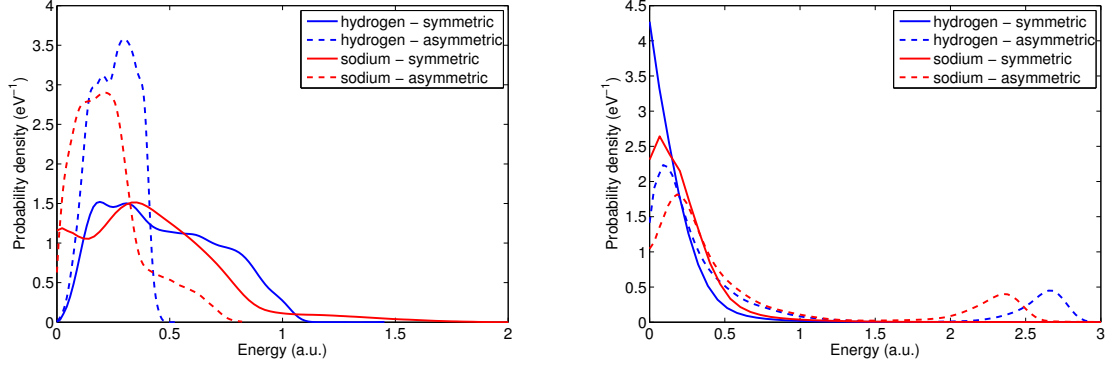


Figure 4.18: Energy distribution of free electrons initially bound in the  $n = 9$  state in hydrogen and sodium atoms.  $dP/dE$  (atomic units) versus electron energy (eV). Incident field strength are: Left figure shows weak field -  $\sim 50\%$  ionization (hydrogen -  $E = 130$  kV/cm, sodium -  $E = 125$  kV/cm). Right figure shows strong field,  $\sim 100\%$  ionization (hydrogen -  $E = 250$  kV/cm, sodium -  $E = 240$  kV/cm).

We see from figure 4.19 and 4.20 that as the initial state  $n$  increases, the difference between simulations of hydrogen and sodium decreases. For  $n = 15$  the probability density has nearly converged on the same values. As mentioned before, this is due to the potential used to represent the sodium atom. As the initial orbital radius  $r$  for the electron becomes large the sodium potential will resemble the hydrogen potential.

We also observe that as the binding energy of the active electron becomes weaker the final energies decrease. There are several possible reasons for this. A small binding energy means that the electron will escape the core faster, and so  $t_{free}$  will be closer to  $t_{min}$ . From equation (4.6) we see that this means a lower final energy. Furthermore, weaker fields that are used to ionize these atoms with a higher initial  $n$ ; weaker fields will transfer less momentum to the electrons. Lastly, the electrons orbiting at the larger radius of the relatively high  $n$  states will be less prone to interacting with, and scattering off, the core of the atom.

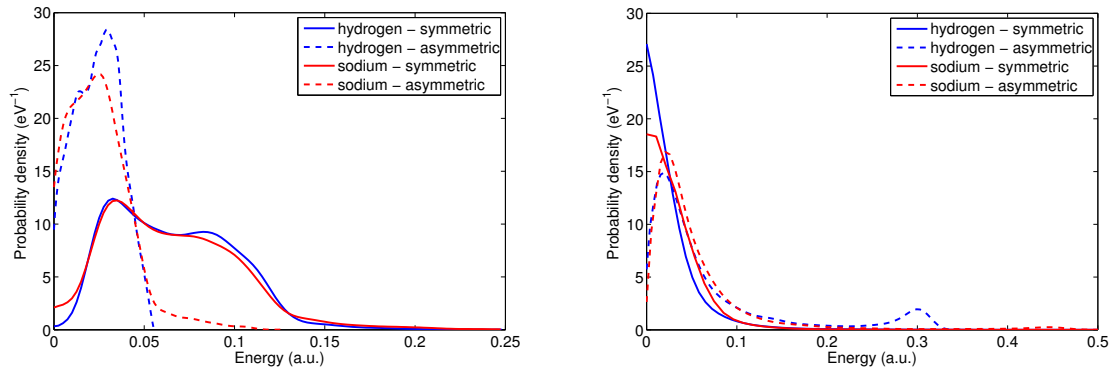


Figure 4.19: Energy distribution of free electrons initially bound in the  $n = 12$  state in hydrogen and sodium atoms.  $dP/dE$  (atomic units) versus electron energy (eV). Incident field strength are: Left figure shows weak field -  $\sim 50\%$  ionization (hydrogen -  $E = 45$  kV/cm, sodium -  $E = 85$  kV/cm). Right figure shows strong field,  $\sim 100\%$  ionization (hydrogen -  $E = 85$  kV/cm, sodium -  $E = 100$  kV/cm).

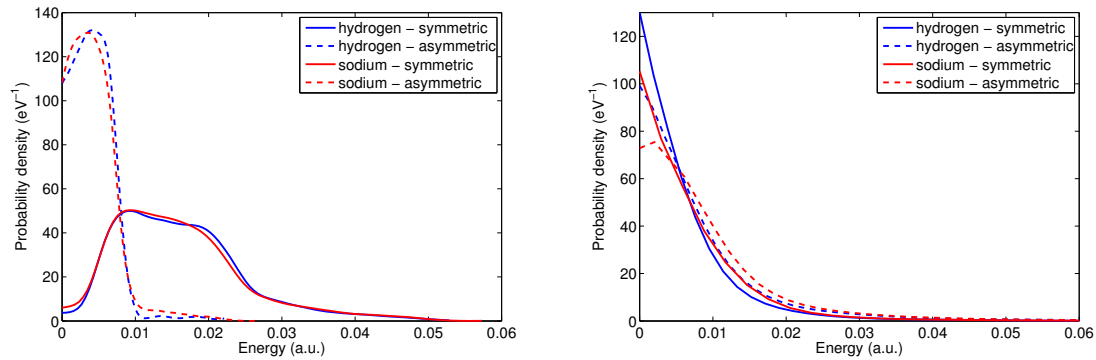


Figure 4.20: Energy distribution of free electrons initially bound in the  $n = 15$  state in hydrogen and sodium atoms.  $dP/dE$  (atomic units) versus electron energy (eV). Incident field strength are: Left figure shows weak field -  $\sim 50\%$  ionization (hydrogen/sodium -  $E = 20$  kV/cm). Right figure shows strong field,  $\sim 100\%$  ionization (hydrogen/sodium -  $E = 60$  kV/cm).

The effects and mechanisms of core scattering are harder to quantize than the effects of the field. This scattering is likely influencing the ionization probability and thus the energy distribution of the various ensembles. In figure 4.19, on the right, we observe that out of the two graphs (green and red) corresponding to the asymmetric pulse, only the one representing hydrogen exhibits a clear peak for a relatively high energy. A possible explanation for this is that the hydrogen potential will more easily allow for core

scattering than the sodium potential, thus allowing electrons in the hydrogen potential to escape at times when the electrons in the sodium potential will not; this in turn leads to the observed difference in the energy distribution.

### 4.2.5 Temporal Behaviour

In this section we examine the change in the space and momentum distribution of the electrons from ionized states while the field is on. Data points at a given time are averages of  $10^5$  simulations and are denoted  $\langle z \rangle$  for the spatial  $z$  coordinate and  $\langle p_z \rangle$  for the momentum  $z$  coordinate.  $\langle x \rangle$ ,  $\langle y \rangle$ ,  $\langle p_x \rangle$  and  $\langle p_y \rangle$  are uniformly distributed and for most simulations small relative to the  $z$ -coordinates. Additionally, the incident field is polarized in the  $z$ -direction. For these reasons we consider only the  $z$ -coordinates. Symmetric pulse shapes are used throughout this section.

We start by showing calculations for the spatial and momentum expectation values for hydrogen in various  $n$  states with a fixed peak field strength. Next, we consider simulations of lithium and sodium initially in a  $n = 9$  state, under the influence of pulses with various peak field strengths. Percentages seen in legend entries in the figures convey the ionization probability of the given system for the relevant field strength of the pulse. The angular momentum of the initial states is distributed as seen in section 3.2.5.

The results of the calculations from section 3.3.1, specifically equations (3.43) and (3.41) are plotted alongside the values for the dynamics obtained by CTMC calculations in figures 4.21 and 4.22, which show the expectation values for the  $z$ - and the  $p_z$ -coordinate, respectively, of electrons from ionized hydrogen atoms versus time. The peak field strength for all calculations in figures 4.21 and 4.22 is  $E = 600$  kV/cm.

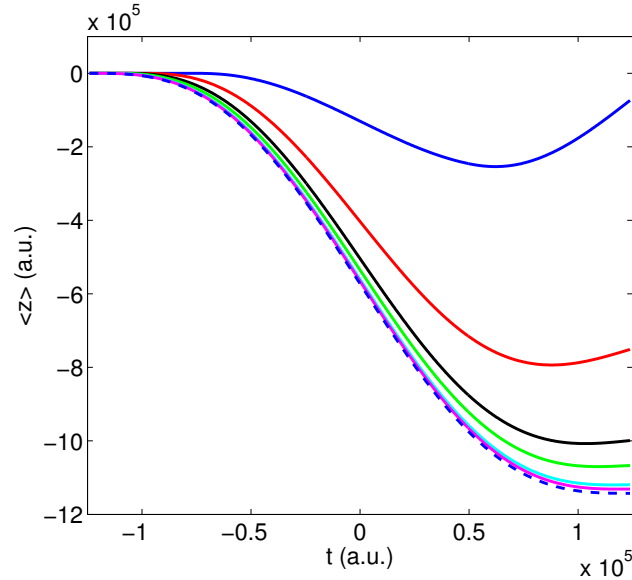


Figure 4.21:  $\langle z \rangle$  versus time for hydrogen initially in an  $n$  state where  $n \in \{6 \text{ (blue)}, 7 \text{ (red)}, 8 \text{ (black)}, 9 \text{ (green)}, 12 \text{ (cyan)}, 15 \text{ (pink)}\}$ . In all these simulations the peak field strength of the symmetric incident field is  $E = 600$  kV/cm. The dashed blue line shows the result of calculating  $z$  from equation (3.43).

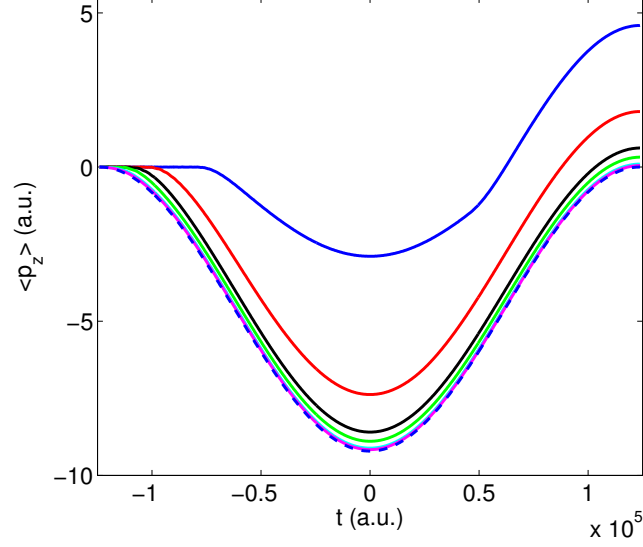


Figure 4.22:  $\langle p_z \rangle$  versus time for hydrogen initially in an  $n$  state where  $n \in \{6 \text{ (blue)}, 7 \text{ (red)}, 8 \text{ (black)}, 9 \text{ (green)}, 12 \text{ (cyan)}, 15 \text{ (pink)}\}$ . In all these simulations the peak field strength of the symmetric incident field is  $E = 600 \text{ kV/cm}$ . The dashed blue line shows the result of calculating  $p_z$  from equation (3.41).

The hydrogen atoms are initially in states  $n \in \{6, 7, 8, 9, 12, 15\}$ . The electrons initially in relatively weakly bound states escape the core attraction before the states initially in a lower initial state  $n$ . As a consequence, these electrons will move further for the duration of the of the incident field. We observe that as  $n$  increases, the expectation value  $\langle z \rangle$  gets closer to the  $z$ -coordinate for the free electron obtained from equation (3.43). Similarly, the expectation value  $\langle p_z \rangle$  approaches the value for the  $p_z$ -coordinate of the free electron obtained from equation (3.41).

We see that the initial state of the system influences the final momentum distribution of the electron ensemble. This is in agreement with the results from section 4.2.4 where the relatively loosely bound systems (*i.e.* high  $n$ ) end up with less energetic electrons than the electrons from relatively tightly bound systems (*i.e.* low  $n$ ). The specific momentum distribution from final states of the electron ensembles are shown as surface-plots in section 4.2.4.

Figure 4.23 shows the average  $z$  position of the electrons from ionized states versus time. The percentages seen in the legend indicate the ionization probability for the system for the corresponding peak field strength.

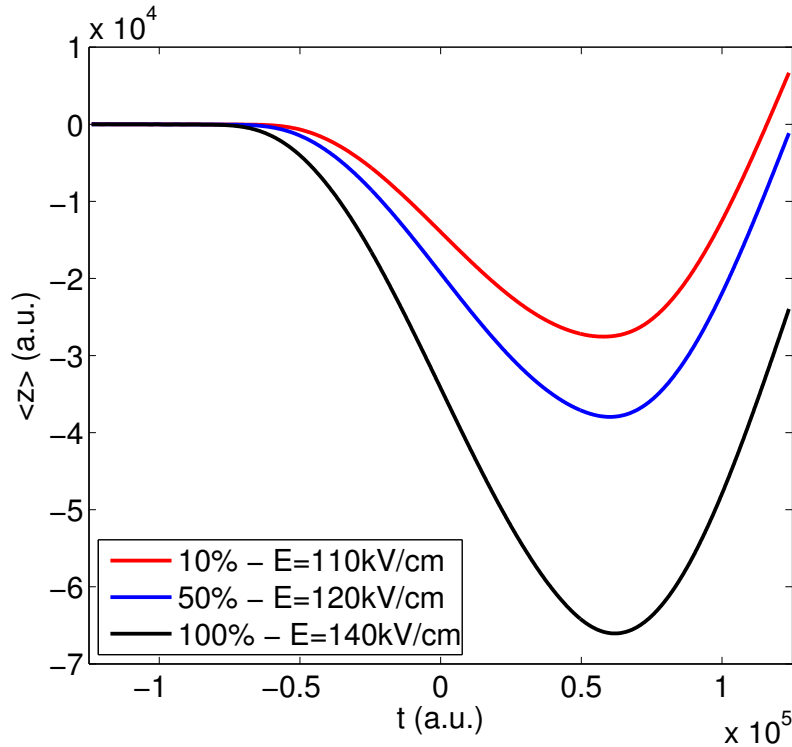


Figure 4.23:  $\langle z \rangle$  as a function of time for the  $H(9d)$  state. Various field strengths are used, where the percentages indicate the ionization probability of the system for the given field strength.

The behaviour resembles that of the free particle, however the electrons are initially bound to the core which restrains the momentum transfer from the field. Electrons in systems subjected to relatively strong fields escape the core attraction first, and will move further in the  $-z$  direction than the electrons in systems subjected to weaker fields. The maximum magnitude for all three systems in this figure is reached at around time  $t = 0.6 \cdot 10^5$ .

In figure 4.24 we see the expectation value of the momentum  $p_z$  versus time for the same electrons as in figure 4.23. As predicted by equation (4.6) the final momentum of these electrons will not be zero as for the free electron. The first half-cycle of the pulse will only be able to transfer momentum to the electrons once they are free, whereas during the second half-cycle of the pulse most electrons will be free and will get the maximum possible momentum transfer when the field is pointing in the  $-z$  direction; this results in a net gain in momentum in the  $+z$  direction for the electrons. Stronger field strengths equate to larger variations in the momentum for the pulse duration, and also a greater net momentum gain. The final distributions of momentum for select states and fields can be seen in section 4.2.6.

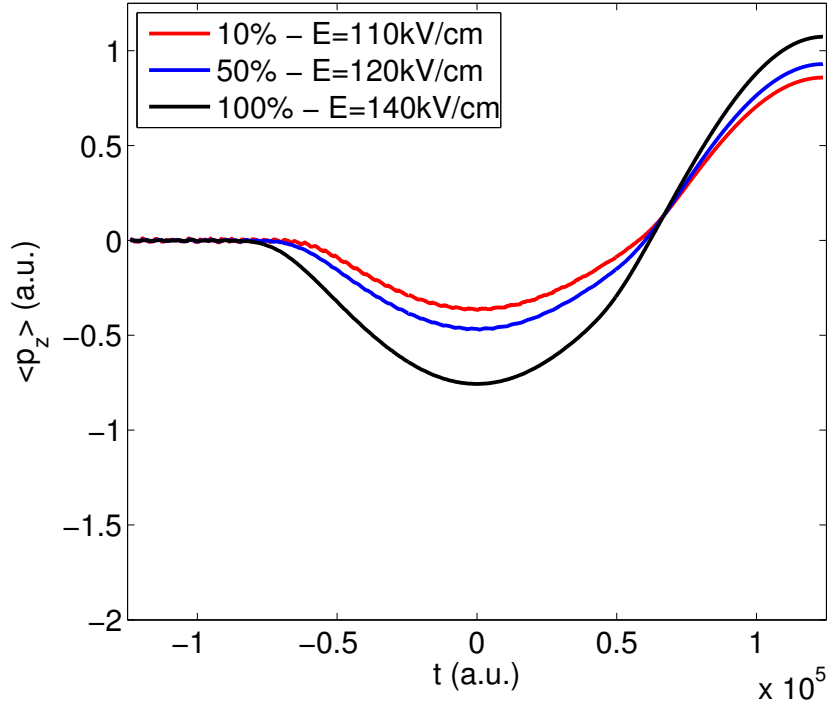


Figure 4.24:  $\langle p_z \rangle$  as a function of time for the  $H(9d)$  state. Various field strengths are used, where the percentages indicate the ionization probability of the system for the given field strength.

Figure 4.25 shows the expectation value for  $z$  (on the left) and  $p_z$  (on the right) for sodium as a function of time. The general behaviour for these elements is similar to that of the hydrogen system; the main difference is the greater variation seen between the states exposed to the various fields. A possible explanation for this is that the electrons escaping these potentials will feel a smaller core attraction when they are close to the core. As explained before, however, the lithium and sodium potentials will be identical to the hydrogen potential for large  $r$ . Similar simulations were done for lithium, but the difference between the lithium and sodium calculations was not great enough to merit another figure for the lithium calculations.

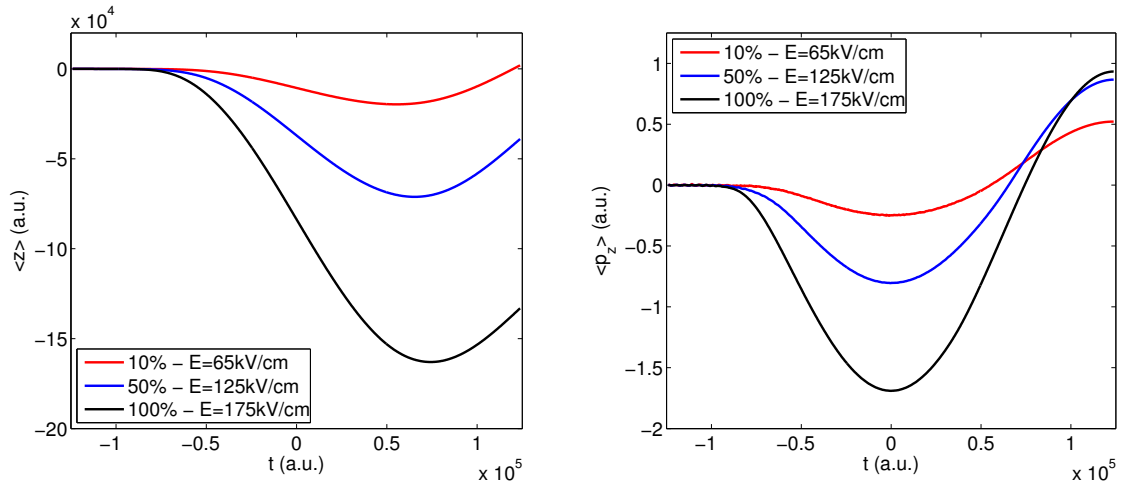


Figure 4.25:  $\langle z \rangle$  and  $\langle p_z \rangle$  as a function of time for the  $Na(9d)$  state.  $\langle z \rangle$  vs  $t$  on the left,  $\langle p_z \rangle$  vs  $t$  on the right. Various field strengths are used, where the percentages indicate the ionization probability of the system for the given field strength.



### 4.2.6 Final State Momentum Distribution

In this section we look at the final spatial and momentum distribution of the electrons from hydrogen atoms initially in various  $n$  states, all subjected to a pulse with a peak field strength  $E = 600$  kV/cm. These final state distributions correspond to the simulations seen in figures 4.21 and 4.22. The color convention used in figures follows the color convention seen in section 4.2.2 and figure 4.8.

Figure 4.26 shows the relative momentum distribution of an ensemble of electrons from hydrogen initially in  $n = 6$  and  $n = 9$  states, after being exposed to a symmetrical field. The final momentum distribution for the states with relatively low  $n$  is pointing in the  $+z$  direction; explanation for this can be found in the two previous subsections. Comparing the two systems, we see that the  $n = 6$  system has on average a larger magnitude of momentum pointing in the  $+z$  direction than the  $n = 9$  system. The momentum distribution in the  $x$  and  $y$  directions are approximately uniform.



Figure 4.26: Surface plots of the relative momentum distribution of the final state of hydrogen initially in  $n = 6$  (left) and  $n = 9$  (right) states. Both simulations are from states subjected to a symmetric pulse with peak field strength  $E = 600$  kV/cm. The blue vertical line indicates  $z$ -axis, in which the field is polarized.

Figure 4.27 shows that when the initial systems are relatively loosely bound, the  $p_x$  and  $p_y$  values become comparable in size to the  $p_z$  values. Final distributions of electrons initially in the state  $n = 12$  is shown on the left, whereas the distribution for electrons initially in  $n = 15$  is shown on the right. We observe that the donut-like shape of the distribution is more pronounced for the  $n = 15$  system. To understand this donut-like shape we must consider how the ensemble of states is initialized and what happens throughout the pulse duration.



Figure 4.27: Surface plots of the relative momentum distribution of the final state of hydrogen initially in  $n = 12$  (left) and  $n = 15$  (right) states. Both simulations are from states subjected to a symmetric pulse with peak field strength  $E = 600$  kV/cm. The blue vertical line indicates  $z$ -axis, in which the field is polarized.

When the systems are initialized the electrons move in bound and stable orbits around the core. In such orbits two of the three momentum components  $p_x, p_y$  and  $p_z$  must be non-zero, which in turn implies that only one of the two components  $p_x$  and  $p_y$  can be zero. The incoming field is polarized in the  $z$  direction, and will not directly influence the momentum components  $p_x$  and  $p_y$ . This means that after the pulse has influenced the system, at least one of the two momentum components  $p_x$  and  $p_y$  must still be non-zero, explaining the donut-like shape seen in figures

### 4.2.7 Individual Electron Trajectories

Meaningful and reliable results from CTMC are results of simulations run on an ensemble of particles. These results are semiclassical in the sense that the ensembles themselves mimic properties of the quantum mechanical wave function. It is still possible, however, to glean certain insights from considering individual electron trajectories. If approached with scepticism, these trajectories may reveal pertinent information about ionization mechanisms. They may provide a path to easier visualization of a certain system.

In this section we consider several single electron trajectories. Most of the simulations are of hydrogen in various states and under the influence of pulses of various intensity. A symmetric field used for all single trajectory simulations. The color convention used in the following graphs is based on the relative electron energy. Blue indicates the minimum energy and red indicates the maximum energy of the electron on the relevant trajectory. Graphs showing the energy of the electron as a function of time are displayed next to all figures in this section, excluding the first one.

Figure 4.28 shows the trajectory of an electron of hydrogen in the state  $n = 6$ ,  $l = 6$  only influenced by the coulomb attraction of the core. When there is no external field present the electron will stay in a stable orbit with constant energy.

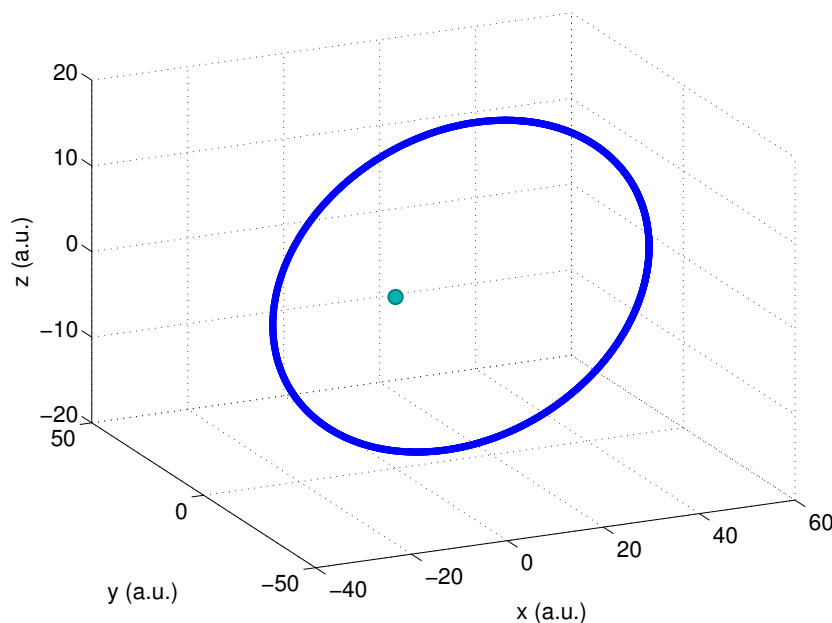


Figure 4.28: Single electron trajectory of hydrogen with no external influence. System is in initial state  $n = 6$ ,  $\ell = 6$ .

Figure 4.29 displays the electron trajectory of a hydrogen atom initially in the state

$n = 6$ ,  $\ell = 4$ . The electron, which has a relatively small orbiting radius, circles the core several times, with energy oscillating with decreasing frequency until it escapes the pull of the core. As seen in previous sections, a stronger field is required for ionization of electrons with relatively low initial  $n$ .

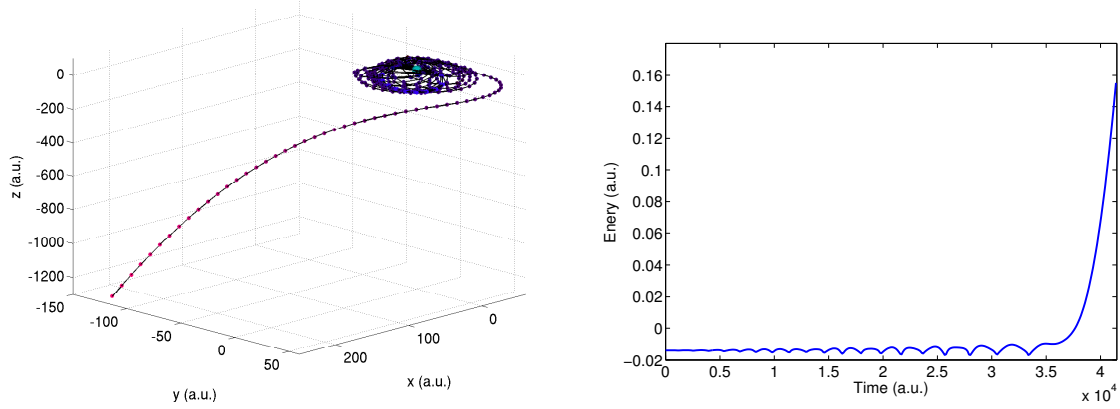


Figure 4.29: Single electron trajectory of hydrogen under influence of a pulse with maximum field strength  $E = 800$  kV/cm on the left and electron energy versus time on the right. System is in initial state  $n = 6$ ,  $\ell = 4$ .

In figure 4.30 we see the electron of an hydrogen atom initially in the state  $n = 9$ ,  $\ell = 2$ . It completes several orbits around the core in which its energy remains pretty much constant. As the field strength increases the electron escapes the core and gradually gains momentum from the field.

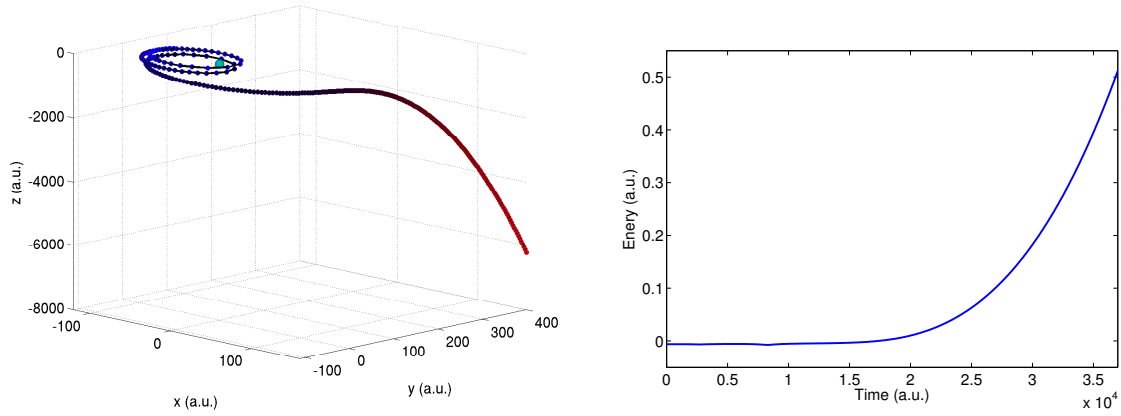


Figure 4.30: Single electron trajectory of hydrogen under influence of a pulse with maximum field strength  $E = 400$  kV/cm on the left and electron energy versus time on the right. System is in initial state  $n = 9$ ,  $\ell = 2$ .

Figures 4.31 and 4.32 display the trajectories and corresponding energies of an electron influenced by a field with strength  $E = 50$  kV/cm and  $E = 300$  kV/cm, respectively. Both the electrons are initially in  $n = 15$  states; the first one with angular momentum  $\ell = 8$ , the second with  $\ell = 10$ . We observe that for systems with a relatively high initial  $n$  the electron may escape after orbiting the core only once, or in the case of the strong field  $E = 300$  kV/cm, before having completed a single orbit.

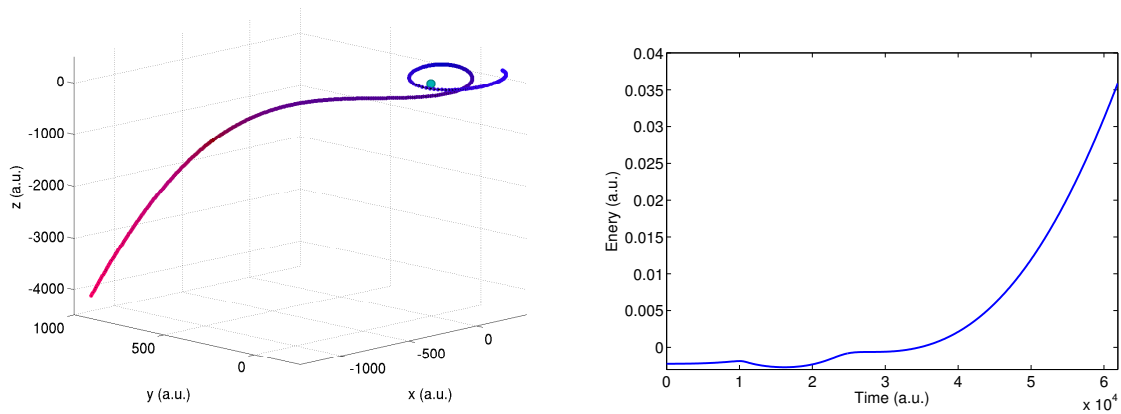


Figure 4.31: Single electron trajectory of hydrogen under influence of a pulse with maximum field strength  $E = 50$  kV/cm on the left and electron energy versus time on the right. System is in initial state  $n = 15$ ,  $\ell = 8$ .

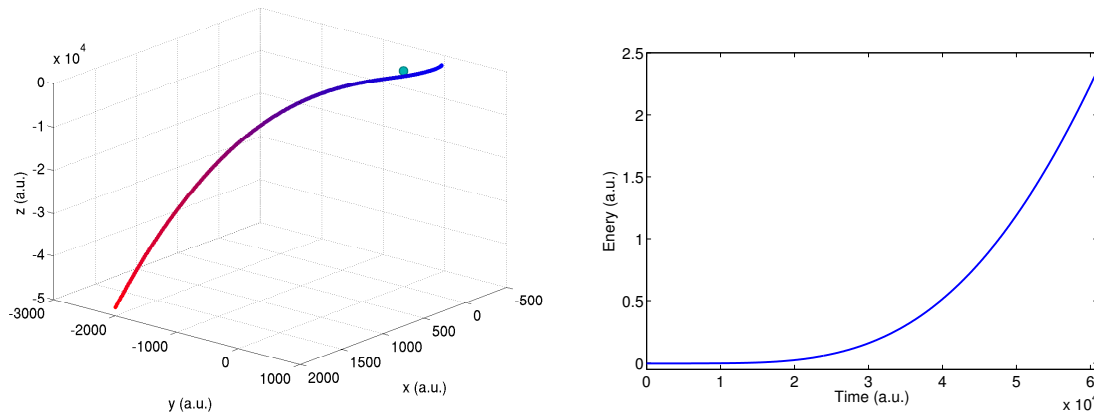


Figure 4.32: Single electron trajectory of hydrogen under influence of pulse with maximum field strength  $E = 300$  kV/cm on the left and electron energy versus time on the right. System is in initial state  $n = 15$ ,  $\ell = 10$ .

In figure 4.33 we see the trajectory of an electron in a sodium atom initially in the state  $n = 9$ ,  $\ell = 8$ . Meaningful observations are harder to make for the slightly more sophisticated sodium potential. We see that the electron orbits the core several time before reaching the required energy for ionization.

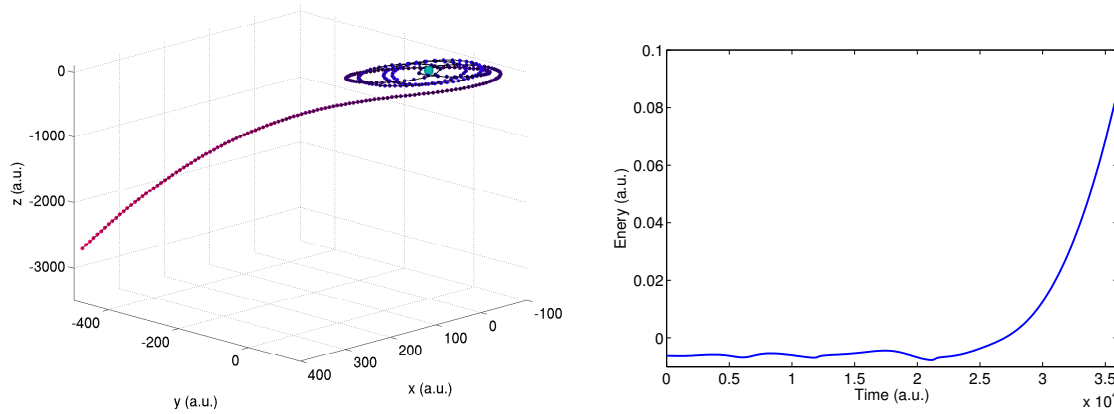


Figure 4.33: Single electron trajectory of sodium under influence of a pulse with maximum field strength  $E = 300$  kV/cm on the left and electron energy versus time on the right. System is in initial state  $n = 9$ ,  $\ell = 8$ .

The ionization probability of electrons with a relatively small orbiting radius (low  $n$ ) is to a larger degree affected by the force from the core than that of electrons with a

relatively large orbiting radius (high  $n$ ). For systems with  $n \simeq 6$  the electron is strongly bound, and its dynamics is heavily influenced by forces due to the proximity to the core. For systems where  $n \geq 12$  a field strength of  $E \approx 30$  kV/cm is enough to rip the electron out of orbit without the assistance of core scattering mechanisms.





## Chapter 5

# Conclusion and Outlook

In this thesis, the influence of single-cycle THz fields on Rydberg atoms have been investigated. The classical trajectory Monte Carlo (CTMC) method, a theoretical approach based on classical mechanics, has been applied to various elements in highly excited states to obtain information about ionization probabilities, electron energy distributions and system dynamics. The basic purpose has been to compare computational results with recent experimental results and to extend the analysis to regimes beyond current experimental results

Quantum mechanical approaches to the problem have been suggested, and demonstrated for 1D systems using a simple model potential. The 3D quantum mechanical simulation faces considerable challenges related to the temporal and spatial size of the relevant systems. The CTMC approach to the same problem evades many of these problems, but can in many cases not be expected to yield correct or precise results.

The ionization probabilities of sodium atoms in  $nd$  states under the influence of asymmetrical THz pulses were calculated and compared with recent experiments [32]. The classical calculations further went beyond the  $n$  range of the experiment and simulations were run for the ionization probabilities of states with very high initial  $n$ . The ionization probabilities of states with various initial angular momentum  $\ell$  was also considered. The energy distributions from ionized states were compared with experiment. Further calculations were done for electrons from hydrogen and sodium atoms with various initial  $n$  and for symmetric and asymmetric fields. We compared the momentum and position for the electrons from ionized states as a function of time. Finally we considered the dynamics of single electron trajectories.

Certain findings are worth accentuating: Classical calculations on ionization probabilities reproduce experimental scaling  $n^{-3}$  for low ionization probabilities, but the results diverge for higher ionization probabilities. The experimental results keep the  $n^{-3}$  scaling whereas the classical calculations exhibit a  $n^{-4}$  behaviour indicative of classical over-the-barrier ionization. The  $n^{-3}$  scaling at lower ionization probabilities is not fully understood, but core scattering mechanisms are thought to play an important role.

Experiment and classical calculations show some agreement in the energy distribution of electrons from ionized states, however classical calculations are unable to reproduce finer details of the experimental distribution. We also see a clear difference in energy distributions when a symmetric field has been applied, versus an asymmetric field. Finally, it was found that electron dynamics in time converges with analytical calculations as  $n$  becomes large;  $\langle z(t) \rangle$  and  $\langle p_z(t) \rangle$  for the electrons follow  $\alpha$  and  $\mathbf{A}(t)$  respectively.

In summary, we have found that CTMC results are in agreement with certain experimental results and trends. The finer details of the experimental results were not reproduced by CTMC (due to shortcomings of the classical approach). The method has proven to be an inexpensive way to produce results that are problematic to obtain through quantum mechanical calculations. The work has lead to an increased understanding of Rydberg atoms subjected to low-frequency single-cycle pulses.

The CTMC method is continuously being developed [37, 38]. The use of several microcanonical ensembles to generate initial distributions that more closely resemble relevant quantum mechanical wave functions may yield better results. Another clear continuation of the work lies in the development of 3D quantum mechanical methods. This has for many years been, and continues to be, an area of active research in the atomic physics group at the University of Bergen.

# Bibliography

- [1] Nicholas Metropolis and Stanislaw Ulam. The monte carlo method. *Journal of the American statistical association*, 44(247):335–341, 1949.
- [2] Roger Eckhardt. Stan ulam, john von neumann, and the monte carlo method. *Los Alamos Science*, 15:131–136, 1987.
- [3] Nicholas Metropolis. The beginning of the monte carlo method. *Los Alamos Science*, 15(584):125–130, 1987.
- [4] J. Hirschfelder, H. Eyring, and B. Topley. Reactions Involving Hydrogen Molecules and Atoms. *The Journal of Chemical Physics*, 4(3):170, 1936.
- [5] Michal Gryzinski. Classical theory of Electronic and Ionic Inelastic Collisions. *Physical Review*, 115:374, 1959.
- [6] R Abrines and I C Percival. Classical theory of charge transfer and ionization of hydrogen atoms by protons. *Proceedings of the Physical Society*, 88:861–872, 1966.
- [7] VI Ochkur and AM Petrun'kin. The classical calculation of the probabilities of excitation and ionization of atoms by electron impact. *Opt. Spectry.(USSR)(English Transl.)*, 14, 1963.
- [8] Robert C Stabler. Classical impulse approximation for inelastic electron-atom collisions. *Physical Review*, 133(5A):A1268, 1964.
- [9] C.O. Reinhold and C.A. Falcón. Classical ionization and charge-transfer cross sections for  $(H^+) + He$  and  $(H^+) + (Li^+)$  collisions with consideration of model interactions. *Physical Review A*, 33(6):3859–3866, 1986.
- [10] Daniel Kleppner, Michael G Littman, and Myron L Zimmerman. Highly excited atoms. *Scientific American*, 244(5):130–149, 1981.
- [11] Thomas F Gallagher. *Rydberg atoms*, volume 3. Cambridge University Press, 2005.

- [12] B.H. Bransden and C.J. Joachain. *Physics of atoms and molecules*. Pearson Education, second edition, 2003.
- [13] Erwin Schrödinger. Quantisierung als eigenwertproblem. *Annalen der physik*, 385(13):437–490, 1926.
- [14] J Clerk Maxwell. A dynamical theory of the electromagnetic field (1865). *The Scientific Papers of James Clerk Maxwell*, 2, 1890.
- [15] James Clerk Maxwell. On physical lines of force, 1861. *A dynamical theory of the electromagnetic field*, pages 1875–89, 1865.
- [16] David Jeffrey Griffiths and Reed College. *Introduction to electrodynamics*, volume 3. prentice Hall Upper Saddle River, NJ, 1999.
- [17] E Merzbacher. Quantum mechanics 3rd edition, 1998.
- [18] Wolfgang Pauli and Markus Fierz. Zur theorie der emission langwelliger lichtquanten. *Il Nuovo Cimento*, 15(3):167–188, 1938.
- [19] HA Kramers. see collected scientific papers, 1956.
- [20] Per Christian Hemmer. *Kvantemekanikk*. Tapir, 2005.
- [21] Walter Gautschi. *Numerical analysis*. Springer Science & Business Media, 2011.
- [22] Michael S Pindzola and David Robert Schultz. Time-dependent lattice methods for ion-atom collisions in cartesian and cylindrical coordinate systems. *Physical Review A*, 77(1):014701, 2008.
- [23] Ladislav Kocbach. Unpublished lecture notes (1999-2015).
- [24] André Stefanov, Nicolas Gisin, Olivier Guinnard, Laurent Guinnard, and Hugo Zbinden. Optical quantum random number generator. *Journal of Modern Optics*, 47(4):595–598, 2000.
- [25] George Marsaglia. Fortran rng - random number generator.
- [26] V Fock. Zur theorie des wasserstoffatoms. *Zeitschrift für Physik*, 98(3-4):145–154, 1935.
- [27] R Abrines and I C Percival. A generalized correspondence principle and proton-hydrogen collisions. *Proceedings of the Physical Society*, 88:873–883, 1966.
- [28] Haruhide Miyagi and Lars Bojer Madsen. Time-dependent restricted-active-space self-consistent-field singles method for many-electron dynamics. *The Journal of chemical physics*, 140(16):164309, 2014.

- [29] Haruhide Miyagi and Lars Bojer Madsen. Time-dependent restricted-active-space self-consistent-field theory for laser-driven many-electron dynamics. *Physical Review A*, 87(6):1–12, 2013.
- [30] S Bauch, L K Sørensen, and L B Madsen. Time-dependent generalized-active-space configuration-interaction approach to photoionization dynamics of atoms and molecules. 062508:1–19, 2014.
- [31] SE Nielsen, JP Hansen, and A Dubois. Electron transfer in kev li+-na (3s, 3p) collisions. i. atomic basis coupled-channel calculations. *Journal of Physics B: Atomic, Molecular and Optical Physics*, 28(24):5295, 1995.
- [32] Sha Li and R R Jones. Ionization of Excited Atoms by Intense Single-Cycle THz Pulses. *Physical Review Letters*, 143006(April):1–5, 2014.
- [33] Lawrence F Shampine and Marilyn Kay Gordon. *Computer solution of ordinary differential equations: the initial value problem*. WH Freeman San Francisco, 1975.
- [34] B. C. Yang and F. Robicheaux. Field-ionization threshold and its induced ionization-window phenomenon for Rydberg atoms in a short single-cycle pulse. *Physical Review A*, 90:1–5, 2014.
- [35] BC Yang and F Robicheaux. Field ionization of rydberg atoms in a single-cycle pulse. *Physical Review A*, 91(4):043407, 2015.
- [36] Ladislav Kocbach. Personal communication.
- [37] LF Errea, F Guzmán, Clara Illescas, L Méndez, B Pons, A Riera, and J Suárez. Electron capture and ionization in collisions of multiply charged ions with h (2s). In *Journal of Physics: Conference Series*, volume 58, page 203. IOP Publishing, 2007.
- [38] DJW Hardie and RE Olson. Charge transfer and ionisation processes involving multiply charged ions in collision with atomic hydrogen. *Journal of Physics B: Atomic and Molecular Physics*, 16(11), 1983.